

Ni- and Co-struvites: Revealing crystallization mechanisms and crystal engineering for phosphorous and transition metal recovery

Stephanos Karafiludis^{1*}, Ana Guilherme Buzanich¹, Zdravko Kochovski², Ines Feldmann¹, Franziska Emmerling^{1,3}, and Tomasz M. Stawski^{1**}

Keywords: struvite; nickel; cobalt; phosphate; phosphorous recovery; crystallization

¹Federal Institute for Materials Research and Testing, Richard-Willstätter-Straße 11, 12489 Berlin, Germany

²Department for Electrochemical Energy Storage, Helmholtz-Zentrum Berlin for Materials and Energy, Hahn-Meitner Platz 1, 14109 Berlin, Germany

³Department of Chemistry, Humboldt-Universität zu Berlin, Brook-Taylor-Straße 2, 12489 Berlin

Stephanos Karafiludis: <https://orcid.org/0000-0002-7257-6311>;

Ana Guilherme Buzanich: <https://orcid.org/0000-0001-5543-9924>;

Zdravko Kochovski: <https://orcid.org/0000-0001-8375-0365> ;

Ines Feldmann: <https://orcid.org/0000-0003-2650-9270> ;

Franziska Emmerling: <https://orcid.org/0000-0001-8528-0301>;

Tomasz M. Stawski: <https://orcid.org/0000-0002-0881-5808>;

Corresponding authors: **tomasz.stawski@bam.de; *stephanos.karafiludis@bam.de

Abstract

Wastewaters containing high concentrations of NH_4^+ , PO_4^{3-} and transition metals are environmentally harmful and toxic pollutants. At the same time phosphorous and transition metals constitute valuable resources. Typically, separate pathways have been considered to extract hazardous transition metals or phosphate, independently from each other. Investigations on the simultaneous removal of multiple components have been studied only to a limited extent. Here, we report the synthesis routes for Co- and Ni-struvites ($\text{NH}_4\text{MPO}_4 \cdot 6\text{H}_2\text{O}$, $\text{M} = \text{Ni}^{2+}$, Co^{2+}), which allow for P, ammonia and metal co-precipitation. By evaluating different reaction parameters, which are representative for some common wastewater compositions, the phase and stability of transition metal struvites, as well as their crystal morphologies, and sizes could be optimized. Ni-struvite is stable in a wide reactant concentration range and at different metal/phosphorus (M/P) ratios, whereas Co-struvite only forms at low M/P ratios. Detailed investigations of the precipitation process using ex situ and in situ techniques provided insights in the crystallization mechanisms. Ni- and Co-struvites crystallize via intermediate colloidal nanophases which subsequently aggregate and condense to final crystals after extended reaction times. This mechanism is different from the practically immediate crystallization of micrometer-sized crystals of ordinary struvite ($\text{NH}_4\text{MgPO}_4 \cdot 6\text{H}_2\text{O}$), which does not seem to involve any amorphous precursor phase. The achieved level of control over the morphology and size, makes precipitation of transition metal struvites a promising method for wastewater treatment. The crystals can be potentially up-cycled into precursor raw materials e.g. for electrochemical or (electro)catalytical applications.

Introduction

The recovery and recycling of critical and essential elements has crucial importance for maintaining of sustainable use of raw materials. Phosphorus is an important, yet, limited natural resource. It is widely used in modern agriculture, mainly in fertilizers, but this element is not fully recyclable. In the mid-term future it could be potentially depleted as a raw material due to the high demand and rapidly declining natural phosphorite ore deposits^{1, 2}. Thus, phosphate rocks are included in the European Union's list of critical raw materials (CRMs)³. At the same time, due to the incomplete P-cycle in nature⁴, phosphorous also causes major problems to the environment such as eutrophication of aquatic systems and is effectively lost for use. Therefore, due to simultaneous scarcity and abundance, the phosphorus recovery from agricultural, industrial, mining, or urban wastewaters have been an important factor in sustaining our global consumption and preservation of the natural environment.

In general terms phosphorous recovery relies on precipitation of P-bearing mineral phases^{5, 6}. Therefore, phosphorous recovery cannot be conducted without considering the presence and the "co-recovery" of metal counter-ions. Alkaline earth metals are ubiquitous, and as such are neither of any particular interest, nor do constitute an environmental risk. In contrast, many d-block-elements are likely pollutants and/or valuable resources. These factors are especially important in the case of the controlled precipitation/crystallization of struvite from wastewater which is already a promising P-recovery route. Struvite is $\text{NH}_4\text{MPO}_4 \cdot 6\text{H}_2\text{O}$, where M^{2+} is Mg^{2+} , but other divalent cations such as Ni^{2+} , Co^{2+} , Zn^{2+} , Cu^{2+} can substitute Mg^{2+} in the struvite structure due to similar ionic radii⁷⁻¹⁰. These recovered M-struvites, with $\text{M} = \text{Ni}$ and/or Co , could act as storage materials for transition metals that may be potentially up-cycled for industrial applications as raw materials for transition metal phosphate (electro)catalysts¹¹⁻¹⁴. While the synthesis of Mg-struvite is sufficiently understood^{15, 16} and used in practice¹⁷, investigations of crystallization of transition metal struvites are scarce. Most of these studies focus on the incorporation of transition metals¹⁸⁻²¹ or other components²² majorly through adsorption rather than the complete substitution of magnesium in the struvite structure^{18, 23-25}. Although, transition metal struvites share their fundamental crystal structure with Mg-struvite, their crystallization pathways, growth kinetics, thermodynamic stability or transformations differ among each other and from for the parent compound, Mg-struvite^{26, 27}. In transition metal phosphate recovery routes aimed at potential up-cycling, the holistic approach towards the crystallization routes is crucial. The goal is to obtain a given phase, but it should also exhibit engineered or at least predictable properties such as crystal size, shape, aspect ratio etc. Crystal engineering of a desired chemical compound determines its performance and scalability in industrial applications. Here, we present the effect of physicochemical conditions of aqueous solutions onto the precipitation of Ni- and Co-struvites. The chosen conditions closely match those typical for several wastewater compositions (see SI). Our findings are compared with the parent Mg-struvite. We highlight the systematic differences in crystallization pathways of Ni- and Co-struvite at all stages. The stability and speciation of the precursor phases is linked to the overall evolution of struvite crystals. The optimized reaction conditions lead to efficient M-struvite precipitation, and therefore to significantly improved phosphorous and transition

metal recovery out of wastewaters. Based on these results tailor-made precursor materials for specific applications e.g. catalysis could be potentially realized ^{13, 14, 22, 28}.

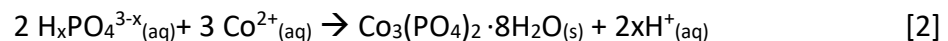
Methods

Synthesis

(NH₄)₂HPO₄ (DAP) (ChemSolute, 99%), MgCl₂·6H₂O, NiSO₄·6H₂O (ChemSolute, 99%) and CoSO₄·7H₂O (Alfa Aesar, 98 %) were used to synthesize metal phosphates under different reaction conditions from 0.004-0.3 M for NiSO₄, CoSO₄ and MgCl₂ and 0.02-0.1 mM for DAP. All detailed reaction conditions are listed in the SI (SI: Table S1). Our work was primarily focused on Ni and Co, but for the sake of comparison we are also synthesized and investigated common struvite (NH₄MgPO₄·6H₂O) at several selected concentrations (SI: Table S1). Based on the above-mentioned concentrations we used the metal-to-phosphate ratios (M/P) ranging for Ni and Mg from 0.02 to 3, and for Co from 0.01 to 3 to characterize each sample. At first 1 M stock solutions of DAP and the metal salts were prepared. The aqueous solutions were made by dissolving the calculated amount of salt in double ionized water (> 18 MΩ·cm). In a simple “one pot” approach, typically 100 ml of DAP and 100 ml of metal-bearing solution were mixed on a magnetic stirrer (300 rpm) at room temperature (25°C). The precipitation reaction of M-struvite was occurring according to the following mass-balance equation (eq. [1]):



Eq. [1] was in general valid for Ni regardless of the metal concentration used, as well as for Co at lower concentrations below a M/P ratio of 0.4. However, at high concentrations of Co²⁺ above a M/P ratio of 0.4 we observed the crystallization of cobalt(II)phosphate octahydrate (CPO) instead of Co-struvite (COS) according to eq. [2]:



To evaluate how the pH influences the crystal morphology, size and stability of M-struvites, sample series of Ni, Co and Mg were synthesized at different initial pH values by adding varying amounts (1-10 ml) of 1 M NaOH_(aq) or 0.1 M H₂SO_{4(aq)}. Here, we used $c(\text{M}^{2+}) = 0.02 \text{ M}$ and $c(\text{DAP}) = 0.1 \text{ M}$ to remain for all chemical systems (Ni, Co and Mg) within the phase stability field of M-struvite. For further analysis, the solid phases precipitated from the mixed solutions were collected onto a cellulose filter (pore size 1 μm, LABSOLUTE) by using a vacuum filtration kit (i.e. Büchner funnel). Afterwards the powders were left to dry in air at room temperature for 2 hours.

Thermodynamic calculations

All the reaction conditions were, prior to the experiments, evaluated and verified by calculations with the aqueous geochemical simulation program PHREEQC ²⁹ using the Lawrence Livermore National Library database (llnl.dat). Missing entries about transition metal struvites in the database were completed with data from Madsen *et. al.* 2017 ³⁰.

pH measurements

The reaction progress was followed in situ by measuring pH as protons were released during precipitation (see eq.[1] and [2]). The pH was continuously measured with a pH electrode connected to a data logger board “DrDAQ” time resolution of 1 s (Pico Technology, Cambridgeshire, UK).

X-ray diffraction

Powder X-ray diffraction (PXRD, XRD) data from the precipitated powders were collected on a D8 Bruker Diffractometer equipped with a LYNXEYE XE-T detector. Diffraction was measured with Cu K α radiation (1.5406 Å, 40 kV and 40 mA) from 5-60° using a step size 0.015° (2 Θ) and a scanning time of 0.5 s per step.

SEM

The scanning electron microscopy (SEM) characterization was conducted on an FEI XL 30 tungsten cathode scanning electron microscope operated at 20 keV and using a secondary electron detector. Prior to the analysis all samples were coated with a 30 nm thick layer of gold.

Dry-TEM

Dry (i.e. particles directly exposed to high vacuum) transmission electron microscopy (TEM) images were obtained on a Talos F200S Microscope (Thermo Fisher Scientific) operating at 200 kV. A Ceta 16M camera (TEM mode) and a HAADF (high-angle annular dark field) detector (STEM mode; Scanning Transmission electron microscopy) were used to capture the images. Additionally, to collect detailed elemental information, energy dispersive X-ray spectroscopy (ED(X)S) was performed by two side-entry retractable silicon drift detectors (SDD). A counting time of 60 s was applied for point measurements while for the elemental maps 40-50 frames were taken resulting in a counting time of 1 hour. The specimen was prepared by mixing the 100 μ l of reactant solutions in an Eppendorf tube (1.5 ml) for 5 seconds of reaction time and dropping 10 μ l of the sample solution onto a 3 mm holey carbon-coated Cu-grid (Lacey Carbon, 400 mesh). Then, the specimens were left to dry at room temperature for 5 minutes.

Cryo-TEM

Under “dry” conditions, due to beam damage and high-vacuum, precipitated phases may develop mesopores similar to what is observed in crystalline struvite after thermal treatment²⁷. Cryo-TEM allowed us to prevent beam damage artefacts of the material. Cryo-EM imaging was performed with a JEOL JEM-2100 transmission electron microscope (JEOL GmbH, Eching, Germany). Specimens were prepared by casting a 4 μ L droplet of sample solution onto lacey carbon-coated copper TEM grids (200 mesh, Electron Microscopy Sciences, Hatfield, PA) and plunge-freezing them into liquid ethane using an FEI vitrobot Mark IV set at 4°C and 95% humidity. Vitrified grids were either transferred directly to the microscope’s cryo-transfer holder (Gatan 914, Gatan, Munich, Germany) or stored in liquid nitrogen. All grids were glow-discharged before use. Imaging was carried out at temperatures around -180°C. The TEM was operated at an acceleration voltage of 200 kV, and an objective lens defocus of about 1.5–2

μm was used to increase the contrast. Micrographs were recorded with a bottom-mounted 4-4k CMOS camera (TemCam-F416, TVIPS, Gauting, Germany). The total electron dose in each micrograph was kept below $20 e^-/\text{\AA}^2$.

X-ray Absorption Spectroscopy (XAS)

To evaluate and compare the metal coordination environments in different phases obtained through synthesis, XANES (near-edge X-ray absorption fine structure) and EXAFS (extended X-ray absorption fine-structure) spectroscopy measurements were performed at the BAMline (BESSY-II, Helmholtz Centre Berlin for Materials and Energy Berlin, Germany)³¹. XANES focusses on the pre-peak and absorption edge features. By analyzing this signal, the oxidation state, the nearest, first coordination sphere and even its degree of distortion can be determined. In contrast, the EXAFS region represents the interaction of the scattered photoelectron on the surrounding atoms of the metal cation. Therefore, the local coordination environment of the surrounding atoms around the metal cation can be evaluated.

The beam was monochromatized using a silicon double-crystal monochromator (DCM) with a crystallographic orientation of [111]. The size of the beam was 3 mm (l) x 1 mm (h). The measurements were performed at Co-K edge (7709 eV) and Ni-K edge (8333 eV) in transmission geometry, with two ionization chambers as detectors. The excitation energy was varied from 7606 eV to 8678 eV for Co and 8230 eV to 9302 eV for Ni, with varying energy steps. For the pre-edge region, the energy was varied in 10 eV steps; for the region around the edge, energy was tuned first in 0.5 eV steps, then in 1 eV steps and in the EXAFS region with a constant step in the k-space of 0.04\AA^{-1} . The associated uncertainties were experimentally determined by measuring the cobalt and nickel metal foils, each 10 times. A value of ± 0.3 eV was obtained for both systems. For the measurement, the samples were mixed with boron nitride, placed in polycarbonate hole plates with a thickness of 1 mm and sealed with a polyimide tape (Kapton) on both sides. Before collecting the sample spectra, a cobalt or nickel foil was used as a reference for the respective K edges. The relative energies of the spectra were calibrated to the first inflection point from the first derivative of the cobalt/nickel metal absorption edge.

The resulting EXAFS data were processed by using ATHENA and ARTEMIS. Both programs belong to the main package IFEFFIT (v. 1.2.11)³². The respective Ni- and Co-phosphates phases were theoretically modelled and fitted to the measured spectra using ARTEMIS. Pre-edge peak areas were determined by Gaussian function fitting and integration after baseline correction. All crystallographic structures were visualized with VESTA (v. 3.5)³³.

Results

The synthesis of transition metal struvites was optimized using different reaction conditions (SI: Tables S1 and S2). The concentrations of the reactant solutions (Mg^{2+} , Ni^{2+} and Co^{2+}) and initial pH values were varied to explore the phase stability field. Concentrations were chosen to be representative for several wastewater types (SI: Table S7 and Supplementary Note).

Phase composition in the transition metal phosphate systems

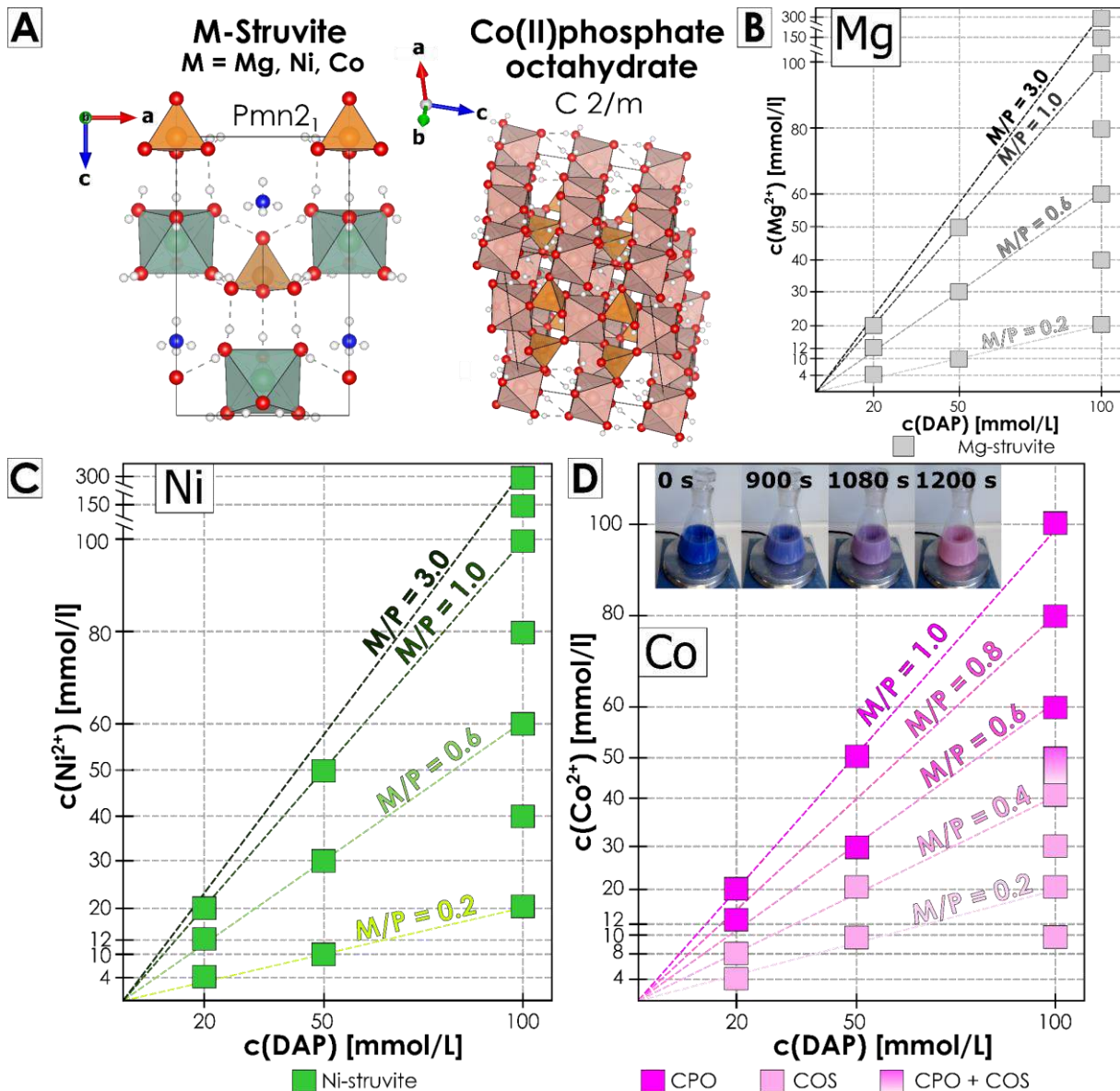


Figure 1: Phase composition diagrams for Mg, Ni, and Co phosphates, which are derived from XRD data presented in the SI (SI: Figure S1); (A) The distinct crystallographic structure of M-struvite $\text{NH}_4\text{MPO}_4 \cdot 6\text{H}_2\text{O}$ (010) plane, M = Mg, Ni, Co and Co(II)phosphate octahydrate $\text{Co}_3(\text{PO}_4)_2 \cdot 8\text{H}_2\text{O}$ is displayed. For (B) Mg and (C) Ni systems, only struvite was observed. For (D) Co a color change of the aqueous solution from blue to purple to light pink at different times can be observed (see inset); The following symbols and abbreviations are used: CPO = $\text{Co}_3(\text{PO}_4)_2 \cdot 8\text{H}_2\text{O}$ cobalt(II)phosphate octahydrate, pakhomovskite; COS = $\text{NH}_4\text{CoPO}_4 \cdot 6\text{H}_2\text{O}$ Co-struvite. Crystal structure colors: white = hydrogen H, blue = nitrogen N, red = oxygen O; orange = phosphorous P; turquoise = metal M = Mg, Ni, Co; pink = cobalt Co; dotted lines hydrogen bonds

We explored the potential phase diagrams in the transition metal/DAP systems of M-struvites, M = Mg, Ni and Co (Figure 1). The data points are derived from the XRD measurements (SI: Figure S1). At all concentration of Mg^{2+} , Ni^{2+} and for all the different M/P ratios, pure single-phase Mg or Ni-struvites ($NH_4MgPO_4 \cdot 6H_2O$, $NH_4NiPO_4 \cdot 6H_2O$) are present (Figure 1B and C). In the Co system at high DAP concentrations of 0.1 M only at a low M/P < 0.4, Co-struvite $NH_4CoPO_4 \cdot 6H_2O$ (ammoniumcobalt(II)phosphate hexahydrate, COS) precipitated as a pure single phase (Figure 1D). At higher M/P > 0.5, cobalt(II)phosphate octahydrate $Co_3(PO_4)_2 \cdot 8H_2O$ (CPO, Co-octahydrate) is formed as the only phase. In the intermediate interval $0.5 > M/P > 0.4$ a binary mixture of CPO and COS is formed (SI: Figure S2A). At lower concentrations of DAP of 0.02 M the transition M/P ratio of Co-struvite to Co-octahydrate is slightly reduced toward lower values below 0.4.

To evaluate how the initial pH impacts the phase stability of M-struvites, different amounts (1-10 ml) of 1 M $NaOH_{(aq)}$ and 0.1 M $H_2SO_{4(aq)}$ were added prior to mixing. For all the samples in a pH-series, $c(M^{2+}) = 0.02$ M and $c(DAP) = 0.1$ M were used to ensure, that the crystals formed within the phase stability field of M-struvite, common for all the systems (M = Mg^{2+} , Ni^{2+} , Co^{2+}). Indeed, for all initial pH adjusted samples and independent of the metal used, M-struvites formed as pure single phase (SI: Figure S3A-F). We calculated the final equilibrium state of the solution based on the calculations with PHREEQC (SI: Table S2). The data from the pH-adjusted samples are included in the SI (SI: Figure S1).

Evolution of the precipitation reaction

In both Ni and Mg systems the respective M-struvite formed as a pure single phase regardless of the reactant concentrations (Figure 1). However, in the case of Co at concentrations of $c(Co^{2+}) > 0.4$ M with $c(DAP) = 0.1$ M other phases precipitated. The phase diagrams in Figure 1 reflect only the final close-to-equilibrium outcome of the crystallization experiments. However, it must be further appended by the observations we made during our studies, which hint about the pathways by which the phases formed. The Co-struvite samples spontaneously dehydrated in air to Co-dittmarite $NH_4CoPO_4 \cdot H_2O$ (COD), as it was evidenced by the XRD (ambient lab conditions, 1 to 3 days depending on a concentration 0.004 M (t = 1 d) to 0.4 M (t = 3 d)) and was indicated by a color change from light purple to light pink. Therefore, Co-struvite had to be stored in a mother liquor for further analysis to prevent decomposition. After several minutes the cobalt phosphate phases transformed from amorphous into crystalline which was accompanied by a color change from blue, to purple, to light pink. The time after which the transformation occurred, was highly dependent on the stirring rate, temperature, pH, and concentration of the reactants^{26, 34, 35}. In the Ni-struvite system, we also observed a very short-lived apparent colloidal precursor phase, as was hinted by a smooth color transition from light green to emerald green. On the other hand, in Mg-struvite such early-stage transformations were not apparent within the observational window. All those observations point to complex crystallization pathways of transition metal struvites. They also indicate that the phenomena should be studied from the point of their evolution, and not only the final products, as we indeed present further.

Due to the fact, that the precipitation processes involved the release of protons (see eq.[1] and [2]), we followed the crystallization mechanisms by conducting time-resolved pH measurements. Here, pH was used as a time-resolved proxy for evaluation of the reaction progress and kinetics. Consequently, we measured pH vs. time in equimolar high concentration samples $c(\text{M}) = c(\text{DAP}) = 0.1 \text{ M}$ and low concentration samples $c(\text{M}) = c(\text{DAP}) = 0.02 \text{ M}$ in the mixed solutions for up to 3600 s (Figure 2).

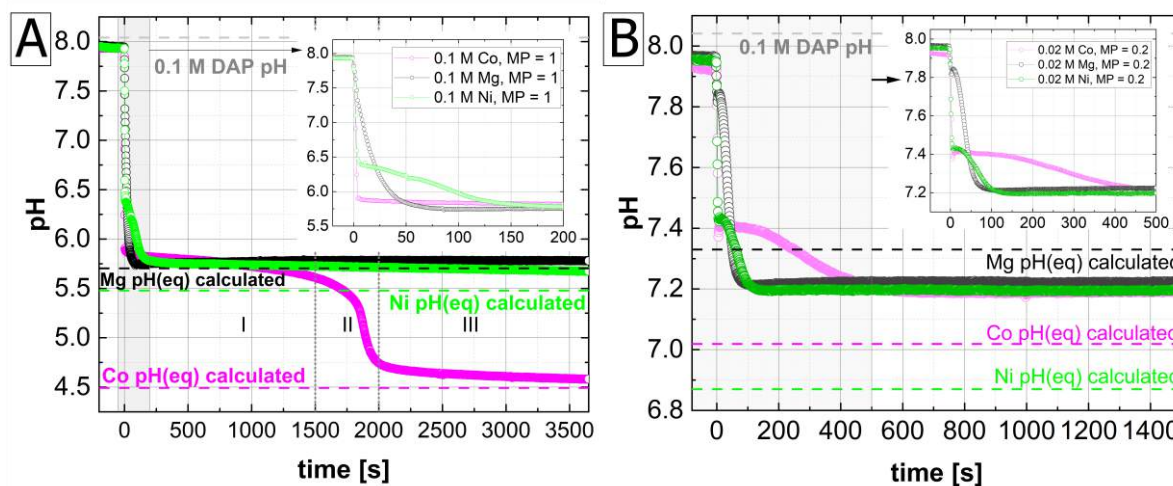


Figure 2: Time-resolved pH measurements with 1 s resolution (A) for the high concentration samples and (B) the low concentration samples; stage I, II, III indicate different slopes in the pH curve of the 0.1 M Co sample; insets show in detail the pH evolution over the first 200 s; the axes in the insets are the same as in the main graphs

The initial pH was ~ 7.9 for the 0.1 M DAP solution and ~ 5.7 for both NiSO_4 and CoSO_4 solutions at 0.1 M, and the 0.1 M MgCl_2 solution exhibited an initial pH of 7.0. When metal salt and DAP equimolar solutions were mixed, near-instant precipitation could be observed in both transition metal systems with the simultaneous drop in pH. On the other hand, the Mg-system had exhibited an induction time of ~ 5 s before it turned turbid. Immediately after mixing both 0.1 M solutions the pH dropped down to around ~ 5.8 for all systems. Here, the color changed within seconds to white-green for Ni and to white-blue/purple for Co. While the pH of the 0.1 M Mg sample declined slightly over the first 50 - 100 s (Figure 1), the pH for 0.1 M Co reached nearly instantaneously a plateau value of 5.9 and was only slightly until around 1500 s, marked by phase I (Figure 2A). After 1500 s a significant pH jump to a value of 4.6 over 500 s occurred in the 0.1 M Co sample marked by phases II and III which was most likely related to the transformation of the colloidal phases as the color changed simultaneously from purple to light pink. The pH of the high concentrated Ni sample dropped first quick (~ 4 s) to 6.4 and declined over 150 s to 5.8. The Mg and Ni sample remained at their plateau value of 5.8.

As Co-struvite is only stable at low Co/P ratios ≤ 0.4 (Figure 1C) additional pH measurements with a M/P ratio of 0.2 were conducted for all systems (Figure 2). The initial pH of the 0.02 M metal solutions was 6.5 (Mg), 5.9 (Ni and Co). The same 0.1 M DAP solution was used as before. Similar trends as in the highly concentrated equimolar solution runs were observed except for Co. In this case, the pH of the Co mixture declined slowly after 450 s to 7.2 and stagnated at this value, as was the case for the other struvite samples. The PHREEQC equilibrium pH calculations are in a relatively close agreement with the experimental values within a confidence interval of $\Delta\text{pH} \approx 0.3$ (see colored dotted lines in Figure 2). That indicates

a progression of the precipitation reaction to completion for all the samples. The deviation between the calculated and measured pH trends, occurred probably due to the presence of amorphous phases, which were difficult to consider in the calculations as barely any (if any) thermodynamic data exist for them.

The Ni- and Mg-struvite formation reaction proceeds fast within the first 100 - 150 s, while the Co-phosphate reactions exhibit much longer reaction times (400 s for 0.02 M and around 3000 s for 0.1 M Co^{2+}) due to the preservation and transformation of long-lived colloidal phases. Therefore, as the colloidal phases affect majorly the kinetics of the precipitation reaction and crystallinity of the final products, it is necessary to investigate them at least at the early stages of nucleation. Especially, from the point of view of crystallization engineering and mechanisms it is questionable if in all these systems the final crystals formed through similar pathways, since phosphates are in general known to form different amorphous phases during crystallization.^{26, 35-38}

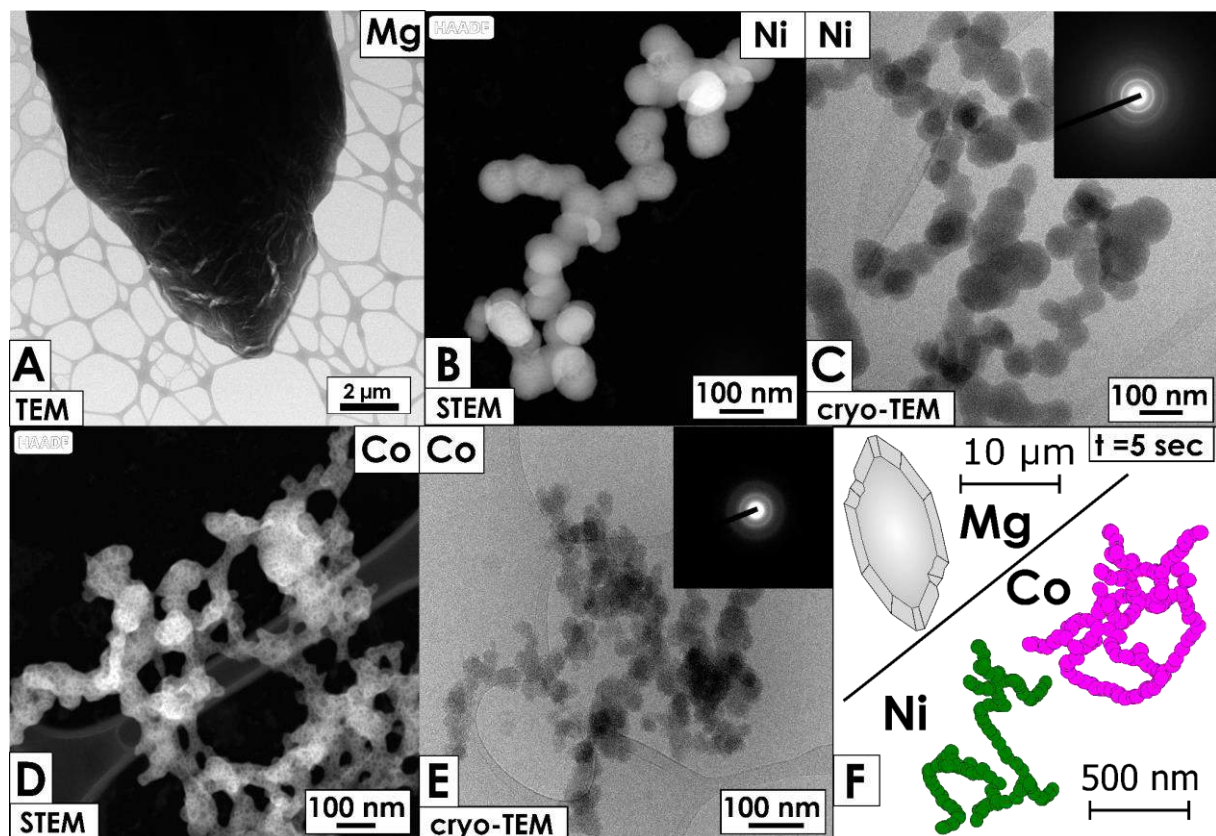


Figure 3: (A) Dry TEM image of a Mg-struvite crystal after 5 seconds of mixing ; (B) dry STEM images of Ni samples after 5 seconds mixing in high angular dark field = HAADF and (C) in cryo-TEM mode with an inset of the SAED pattern; (D) dry STEM images of Co samples after 5 seconds mixing in high angular dark field = HAADF and (E) in cryo-TEM mode with an inset of the SAED pattern; (F) a network of sphere-shaped particles are clearly amorphous; summarizing sketch of the observed features; supporting EDS mappings and point measurements can be found in the SI (SI: Figures S4-S6)

Accordingly, to gain more insight into the formation of the transitional precursor phases during crystallization dry TEM and cryo-TEM measurements combined with EDS mappings and SAED analysis were performed. Each sample was prepared for a reaction time of 5 seconds (Figure 3). The Mg sample showed immediately μm -sized crystals of needle-shaped Mg-struvite apparent to the eye with well-developed crystal planes (Figure 3A and SI: Figure S4).

In contrast to that the Ni- and Co-samples exhibited amorphous round nanoparticles with sizes of around 50 nm and chemical composition very close to M-struvite, which agglomerated to bigger units (Figure 3B-F, SI: Figures S5 and S6). The Ni-nanoparticles and their aggregates appeared more condensed and regular compared to those of Co. Since it is apparent that transition metal struvites differ significantly in their crystallization pathway from Mg-struvite with various temporally occurring amorphous colloidal nanophases (Ni short-lived nanophases for several seconds; Co long-lived nanophases stable up to hours) an analysis of the crystalline precipitate could elucidate how these colloidal phases influence the crystalline particles. Different concentrations of M^{2+} /DAP and initial pH variations could influence the crystalline particles directly. Alternatively, we envisage that the amorphous nanophases could indirectly interact with the already growing crystals in the secondary nucleation processes.

Crystal engineering of transition metal phosphates

To quantify how the concentration changes of transition metal M^{2+} /DAP and initial pH effect the morphology and size of the crystallites, SEM analysis was performed. A strong dependency of the morphology and size of the crystals can be observed in the Ni-system in respect to the M/P ratio (Figure 4A, SI: Figure S7). Ni-struvite morphologies with an M/P ratio ≥ 1 (high $c(Ni^{2+})$ compared to low $c(DAP)$) showed an anhedral rounded appearance and many agglomerated crystal nuclei with a crystallite size of (length from edge-to-edge) 11 ± 3 nm with $c(Ni) = c(DAP) = 100$ mM. At low M/P ratios ≤ 1 (low $c(Ni^{2+})$ compared to high $c(DAP)$) the crystals exhibited a more euhedral elongated X- or “coffin-like” shaped habit with crystallite size of 55 ± 9 nm with $c(Ni) = 20$ mM and $c(DAP) = 100$ mM. The X-shaped habit of the crystals occurred at low M/P ratios < 0.5 and high $c(DAP) \geq 50$ mM while the “coffin-like” morphology appeared at low M/P ratios < 0.5 but at low $c(DAP) \leq 50$ mM. High Ni^{2+} concentrations at a constant DAP concentration favor many crystallites of smaller size with an anhedral appearance while high DAP concentrations at a constant Ni^{2+} concentration increase the crystallite size and idiomorphism of the crystallites. Adding $NaOH_{(aq)}$ and the coupled increase of pH favors the formation of M-struvite as protons are released through the precipitation reaction which counteracts the pH effect of OH^- ions (eq.[1]). Adding $H_2SO_{4(aq)}$ and the coupled decrease of pH inhibits the precipitation of M-struvite as they dissolve with decreasing pH and shifts the chemical equilibrium on the reactants' side (see eq.[1]). Adding $NaOH_{(aq)}$ to the Ni-struvite system alter the crystal morphology strongly and decreased the crystallite size from 50 ± 9 nm to 5 ± 1 nm (grey inset in Figure 4A, SI: Figure S8). In addition, it changes the crystal habit to an orthorhombic prism appearance. Adding $H_2SO_{4(aq)}$ affects the surface of the crystals strongly, although under these conditions the crystallite size and the X-shaped-like morphology are not influenced in comparison with the pH-unadjusted sample at the same M^{2+} and DAP concentrations. All trends in terms of crystal morphology and size for Ni and Co are summarized in the SI (SI: Figure S11).

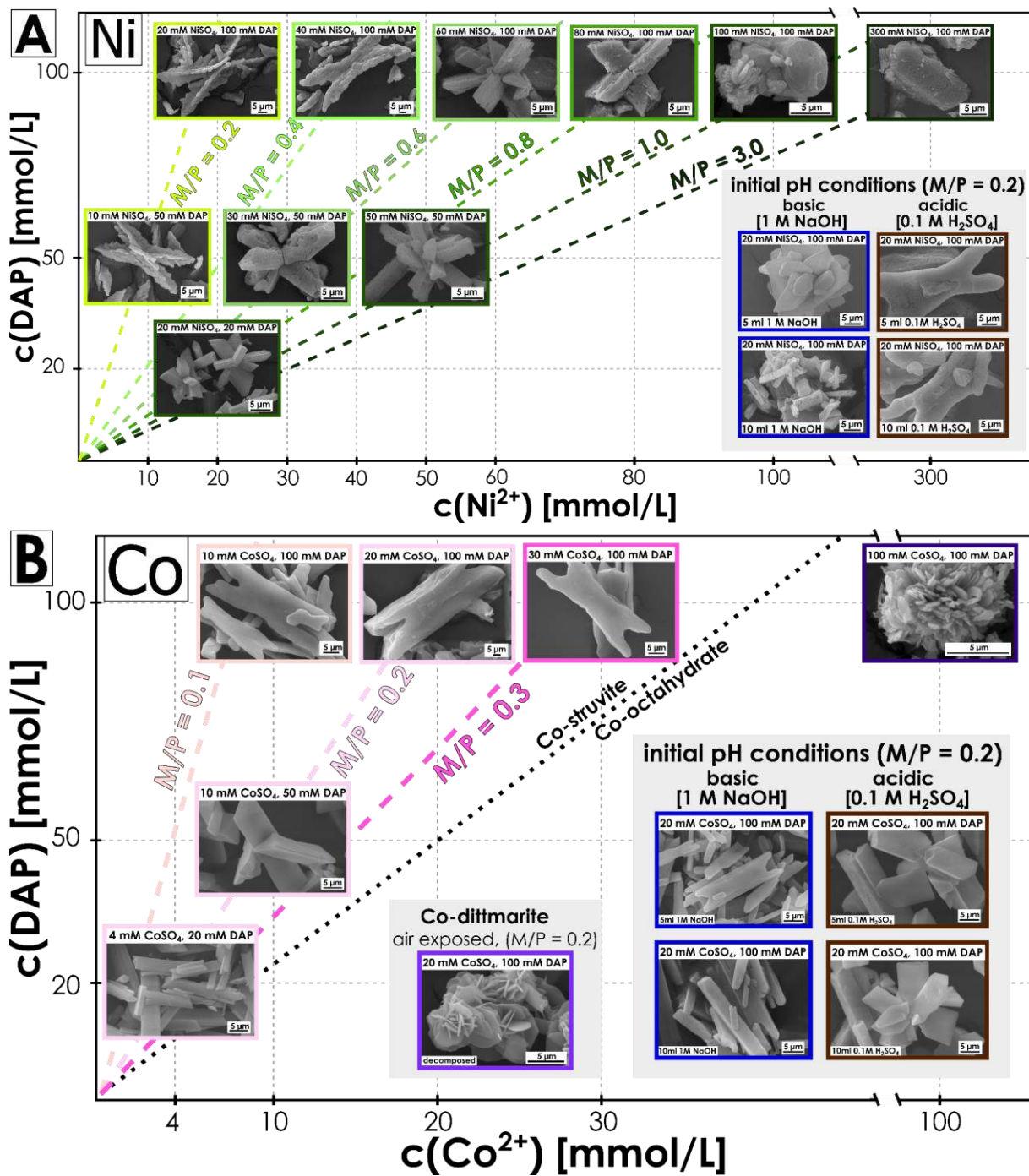


Figure 4: $c(\text{M}^{2+})$ vs. $c(\text{DAP})$ plot with (A) green (for Ni) and (B) pink (for Co); color frames and dotted lines indicate the distinct M/P ratio of the sample; lower right left corner: pH samples with a M/P ratio = 0.2 (0.02 M NiSO₄/CoSO₄, 0.1 M DAP) with different initial amounts of 1 M NaOH_(aq) (blue frames) or 0.1 M H₂SO_{4(aq)} (brown frames); in air Co-struvite decomposed to Co-dittmarite with a M/P ratio = 0.2, and is displayed in (B)

Due to the limited stability of Co-struvite at low M/P ratios, only samples with the ratio below 0.4 could be analyzed. Above the ratio of 0.4 only Co-octahydrate is stable. At a constant ratio the crystallite size increased from $16 \pm 5 \mu\text{m}$ with 4 mM Co²⁺ and 20 mM DAP to $60 \pm 13 \mu\text{m}$ with 20 mM Co²⁺ and 100 mM DAP. The Co system follows a similar, but weaker correlation to the one seen for the Ni. High DAP concentrations favor the formation of large euhedral crystals while higher Co²⁺ contents lead to small anhedronal crystals. Similarly to Ni-struvite, Co-struvite exhibits X-shaped crystal morphologies at high $c(\text{DAP}) \geq 50 \text{ mM}$ and low M/P ratios < 0.3 , but the crystallographic planes are anhedrally developed (Figure 4B, SI: Figure S9). The “coffin-

like” habit occurs at low M/P ratios < 0.3 and low $c(\text{DAP}) \leq 50$ mM. Co-octahydrate shows a rough two-dimensional flake- or sheet-shaped morphology of the crystals and forms big crystal agglomerates of several μm . Co-dittmarite demonstrates a similar habit of regularly arranged plates, also reported in other studies³⁴. By increasing the pH with NaOH the crystal habit changed from a X-shaped morphology to elongated rod or prism-like habit (Figure 4, SI: Figure S10). Here, the 5 ml 1 M NaOH_(aq) sample indicates remarkably the transition between those two morphologies. 10 ml NaOH_(aq) decreased the crystallite size from 60 ± 13 μm to 23 ± 6 μm . Reducing pH by addition of H₂SO_{4(aq)} favors the formation of tabular-shaped Co-struvites with slightly decreased size of 35 ± 8 μm .

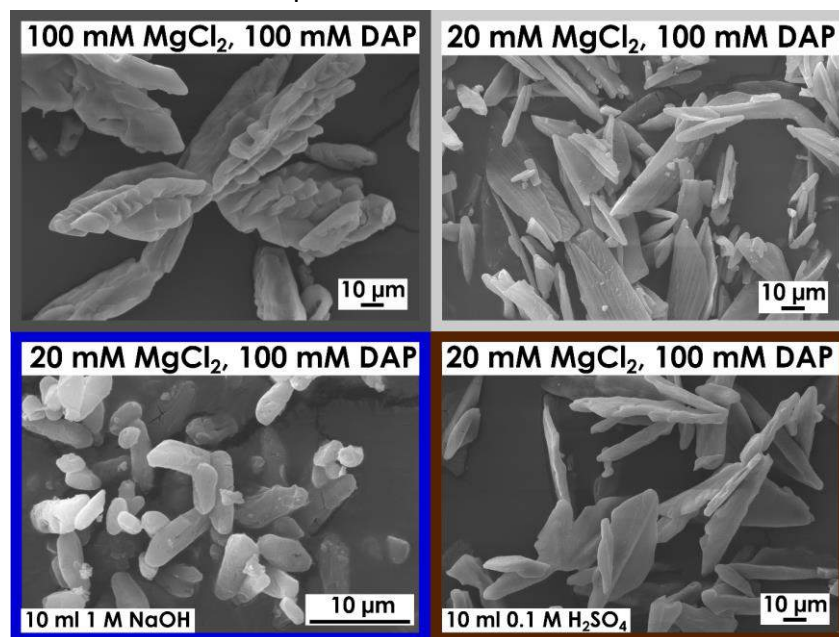


Figure 5: SEM images of different Mg-struvites at low M/P ratios of 0.2 with pH adjusted samples at the sides and one sample with high M/P ratio of 1; frame colors indicate different conditions: dark grey = $c(\text{Mg}^{2+})$ of 0.1 M, light grey = $c(\text{Mg}^{2+})$ of 0.02 M; blue = basic pH conditions of 10 ml 1 M NaOH_(aq); brown = acidic pH conditions with 10 ml 0.1 M H₂SO_{4(aq)}

Mg-struvite is a relatively extensively investigated mineral phase^{27, 36, 39}, and therefore it was synthesized to serve as a reference for transition metal phosphates (see Figure 5, SI: Figure S12). At high concentrations of DAP and Mg²⁺ struvite formed an X-shaped crystal habit with a crystallite size of 120 ± 20 μm , while at low concentrations orthorhombic prisms were observed and the crystallite size decreased to 40 ± 6 μm (see Figure 5, SI: Figure S12). In the case when we adjusted conditions to be initially acidic (adding 10 ml of 0.1 M H₂SO₄ with a pH = 1.00) the struvite crystals were comparable in terms of shape and size to those observed in the pH unadjusted samples. However, the surface exhibited features of acidic leaching. Under basic conditions (adding 10 ml of 1 M NaOH_(aq) with a pH = 13.97), the size of the crystallites got reduced to 5 ± 2 μm and the shape changed to more rounded orthorhombic prisms, but in contrast to acidic conditions the crystal surface were visually not affected. These results already demonstrate a controllable and tunable adjustment of the crystallite size, morphology, and composition of M-struvites through changes in the reaction conditions.

Stability of phases from the point of coordination environment

Crystalline M-struvites form in both transitional metal systems (Ni^{2+} , Co^{2+}), but they exhibit different stability. Co-struvite decomposes in air to Co-dittmarite while Ni-struvite remains stable. These differences can be explained in the context of the local coordination environment of the MO_6 octahedron in the struvite structure. To evaluate how the stability of Ni and Co phosphates is related to their coordination environment in the crystal structure and how they differ between each other, EXAFS measurements were performed on the powder samples. In general, XAS analysis reveal quantitatively changes in oxidation state, in the local coordination geometry/symmetry and bond distances among the different Co- and Ni-phases. Especially the intensity of the pre-peak (XANES) which originates from the $1s\text{-}3d$ transitions expresses the degree of centrosymmetry and coordination environment in the vicinity of the considered ions (Figure 6). As only $3d\text{-}4p$ hybridization enable parity allowed transitions the extent of those is strongly correlated with the coordination geometry. Near-ideal octahedral coordination sites show very low pre-peak intensities due to the presence of an inversion center while more distorted geometries exhibit higher intensities.

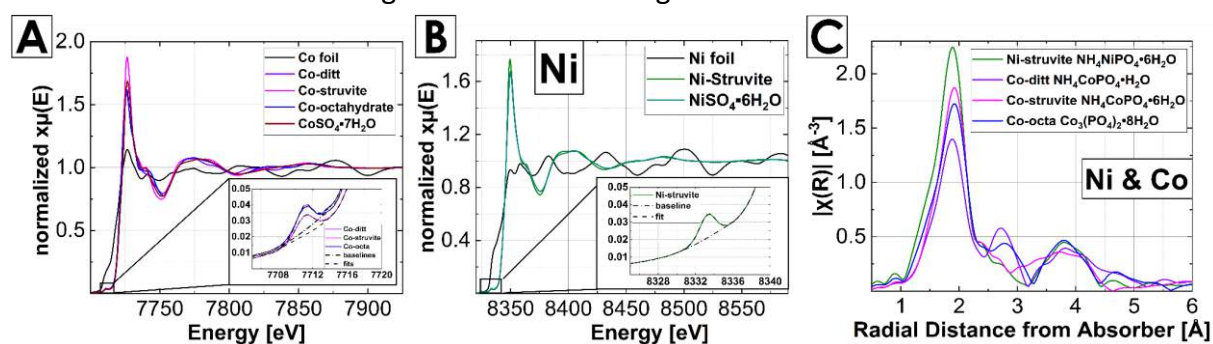


Figure 6: XAS spectra of (A) Co and (B) Ni samples with detailed view of the pre-peak region; (C) Fourier-transformed Ni- and Co spectra plotted in R-space with detailed view of XAS spectrum of Ni-struvite.

Table 1: Pre-peak integration results by fitting Gaussian functions with all fitting parameters

Sample	Prepeak area integration results			fit function: Gaussian		
	chemical formula	R ² value	Pre-peak Area A_{pp} (err)	FWHM	Center	Max. Height
Co-octahydrate	$\text{Co}_3(\text{PO}_4)_2 \cdot 8\text{H}_2\text{O}$	0.995	0.0363(4)	2.296	7711.2	0.0149
Co-dittmarite	$\text{NH}_4\text{CoPO}_4 \cdot \text{H}_2\text{O}$	0.991	0.0355(4)	2.101	7711.5	0.0159
Co-struvite	$\text{NH}_4\text{CoPO}_4 \cdot 6\text{H}_2\text{O}$	0.993	0.0298(3)	2.314	7711.1	0.0121
Ni-struvite	$\text{NH}_4\text{NiPO}_4 \cdot 6\text{H}_2\text{O}$	0.992	0.0281(2)	1.969	8333.3	0.0134

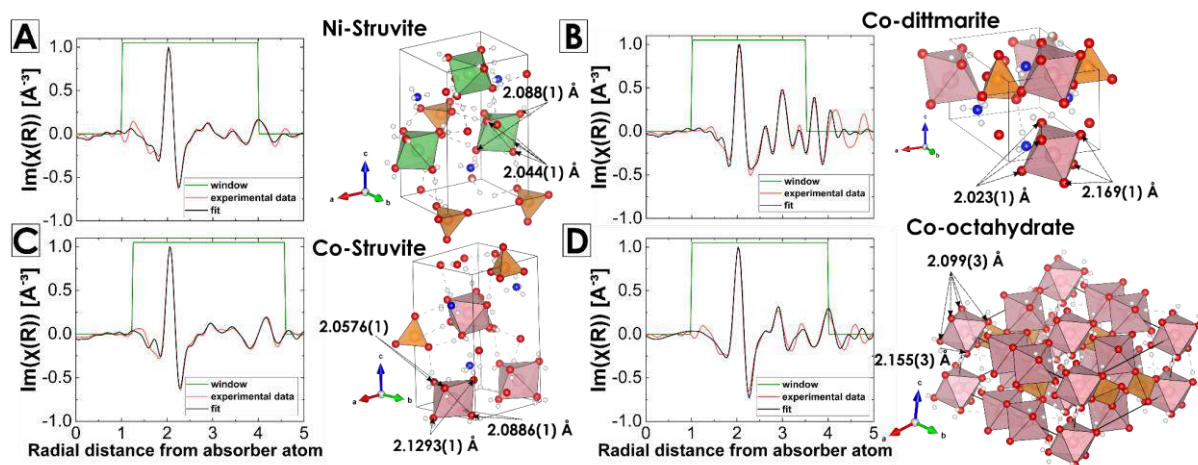


Figure 7: Ni- and Co K-edge EXAFS data shown in real space for (A) $\text{NH}_4\text{NiPO}_4 \cdot 6\text{H}_2\text{O}$ space group: $\text{Pmn}2_1$, $R = 0.005$; (B) for $\text{NH}_4\text{CoPO}_4 \cdot \text{H}_2\text{O}$ space group: $\text{Pmn}2_1$, $R = 0.008$; (C) $\text{NH}_4\text{CoPO}_4 \cdot 6\text{H}_2\text{O}$ space group: $\text{Pmn}2_1$, $R = 0.012$; and (D) $\text{Co}_3(\text{PO}_4)_2 \cdot 8\text{H}_2\text{O}$ space group: $\text{C}2/\text{m}$, $R = 0.005$; experimental data: red, fit results: black; fit window: green.

The XAS spectra (Figure 6) clearly prove that Co and Ni are exclusively present as the bivalent species in all samples, as is evidenced by comparing with multiple M^{2+} standards (only $\text{MSO}_4 \cdot n\text{H}_2\text{O}$ is shown for clarity). No indication for incorporated oxidized Ni^{3+} or Co^{3+} was observed in the powders. Quantitative pre-peak integration results are summarized in Table 1. As it is indicated by a minimal pre-peak area ($A_{\text{pp}} = 0.0298(3)$) and a maximized intensity in the white lines, Co-struvite as well as Ni-struvite ($A_{\text{pp}} = 0.0281(2)$) have a more centrosymmetric octahedral coordination environment compared to Co-dittmarite and Co-octahydrate ($A_{\text{pp}} = 0.0363(4)$ and $A_{\text{pp}} = 0.0355(4)$). After FT of $\chi(k)$ into R-space radial distances from the absorber atom can be observed (Figure 6C). At around $R \approx 1.9 \text{ \AA}$ all samples show a maximum which is related to the degeneracy of single scattering path of the Ni-O or Co-O bond length. In the case of single scattering, we have a direct measure of the coordination number (CN). The peak at $R \approx 2.7 \text{ \AA}$ in CPO and COD fits to the Co-P single scattering path, which is absent in the M-struvites. In CPO and COD the CoO_6 octahedrons are linked to four (CPO) or five (COD) O^{2-} of PO_4 tetrahedrons (short distance of Co-P) while in the struvite structure they are coordinated by the O^{2-} of six water molecules, and therefore are isolated from the phosphate tetrahedron (long distance of Ni-P and Co-P, SI: Figure S13). The slight color change among COS, COD and CPO of the chemical compounds of Co is probably related to how many of the ligands are crystal water molecules: 6 for COS, 5 for COD and 4 for CPO. The peak at $R \approx 3.8 \text{ \AA}$ consists of several single and multiple scattering paths such as Co-N, Co-H, Co-P, Co-O-O.

Quantitative real-space fittings on the radial distribution function reveal the bond distances in the first coordination environment around the Co^{2+} and Ni^{2+} metal cation. All fitting parameters are shown in SI: Tables S3-S6. By calculating the mean bond distance and its sphere volume, a quantitative comparison of the coordination sphere is possible. The M-struvites (M-struvite Ni: $2.059(6) \text{ \AA}$ Co: $2.091(1) \text{ \AA}$) demonstrate slightly lower mean bond distances than COD and CPO (CoD: $2.096(1) \text{ \AA}$, CPO: $2.11(2) \text{ \AA}$). The fitted bond distances are visualized with the calculated fits in Figure 7 for the different compounds (SI: Tables S3-S6).

Discussion

General phase stability and transformations

In all the considered chemical systems crystalline M-struvites could be obtained, but the conditions and the nucleation pathways toward the final crystal varied among different cations. At concentrations of 0.02 M Mg, Ni, and Co formed single-phase M-struvites, in which consequently the ammonium ions were bound in the precipitates. The reduction of the pH represented a combination of adding a slightly acidic solution to the mixture together with the release of protons during the precipitation reaction of M-struvite. At concentrations of 0.1 M Co and 0.1 M DAP, CPO formed through transformation of amorphous phases accompanied by a color change from blue to purple to pink. This transition of colors is highly significant because it points to specific meta-stable reaction products. In CPO, the M/P ratio is 3:2 which leads to unreacted amounts of PO_4^{3-} and NH_4^+ in the aqueous solution due to the absence of M-struvites ($\text{M/P} = 1$), even assuming complete depletion of the reactants in the reaction. As ammonium is the most abundant species in the aqueous solution, the dissociation equilibrium to ammonia with the release of protons dominates the pH. The remaining less abundant phosphate, and the coupled dissociation to $\text{H}_x\text{PO}_4^{3-x}$ species, with the removal of protons can only compensate to a limited extent. It is assumed that the jump of the pH after 1800 s is related partly to the transformation of the amorphous Co phases to crystalline CPO with the release of protons as the color changes from purple to pink in this time interval. Moreover, one should also consider the formation of $\text{Co}(\text{NH}_3)_x\text{H}_2\text{O}_{6-x}^{2+}$ aqua complexes due to the incomplete consumption of Co^{2+} with the additional reduction of the pH through proton release by converting ammonium to ammonia. The light pink color of the residual solution after the precipitation of CPO was a source of this assumption^{40, 41}. The 0.1 M concentrated Ni and Mg samples mixed with 0.1 M DAP do not exhibit any late reduction of pH as most of the ammonium is bound in the struvites, and probably no amorphous metal phosphate phase is stable over a long period (> several mins).

Crystal morphology and phase

In general, the morphology of the crystals observed in SEM is influenced by vacuum, which is indicated by intermittent vacuum-induced cracks. Nevertheless, since all crystals are exposed to the same vacuum influence, the change in morphology should be related to the differences in the experimental conditions. Looking at the ionic radii of $\text{Co}^{2+[\text{VI}]}$ (0.75 Å, high state) and $\text{Ni}^{2+[\text{VI}]}$ (0.69 Å) compared to $\text{Mg}^{2+[\text{VI}]}$ (0.72 Å), all ions have similar radii so they could be potentially substituted one for another in the struvite structure $\text{Pmn}2_1$. Following the formation of the crystals, a higher supersaturation leads to a higher nucleation rate which provides numerous crystal nuclei of smaller crystallite sizes. At low supersaturations only a few crystal nuclei grow significantly due to a lower nucleation rate. Based on observations, the Ni^{2+} and Co^{2+} concentration effects the struvite morphology as a regulator of supersaturation and reaction kinetics, but also as the source for potential metal aqua complexes, which in turn influence the precipitation through positive feedback. Higher concentrations of DAP correlate with the apparent elongation and increasing crystallite size of the crystals at a constant M/P ratio. Similar effects were observed for the crystallization of

Mg-struvites³⁹. As in DAP two moles of NH_4^+ are present, the effect of higher DAP concentrations on the crystals is mostly related to higher concentrations of ammonium. In all systems a reduction of the initial pH by adding $\text{NaOH}_{(\text{aq})}$ decreased the crystallite size significantly and stabilized a more rod/prism-like morphology of the crystals. Upon adding $\text{H}_2\text{SO}_{4(\text{aq})}$ the crystallite size remained practically unchanged in the Ni-system, but the crystal surface was clearly affected by the acid. In the Co-system the crystallite size decreased slightly to $\sim 10 \mu\text{m}$ and the morphology changed to more tabular shapes. The Co-samples treated with sulfuric acid exhibited a short presence of the transitional amorphous colloidal phases of 10-15 mins as well as they decomposed faster to Co-dittmarite within several hours compared to the pH unaffected samples. Here again, Co-struvite demonstrates low stability compared to Ni-struvite. Since only 0.1 M $\text{H}_2\text{SO}_{4(\text{aq})}$ was added initially in the amount sufficient not to dissolve the crystals completely, the absolute change in pH, $|\Delta\text{pH}|$, was lower and asymmetric than the one induced by adding higher concentrated 1 M $\text{NaOH}_{(\text{aq})}$ to the system. As an increase of the pH (i.e. decrease in proton concentration) shifts the equilibrium to the side of the products in eq.[1], a high number of crystal nuclei are formed and grow simultaneously. Consequently, as many crystals of a low size have a higher surface area compared to a few crystals with a big size, these nuclei will grow only to a limited extent. Therefore, these crystals are much smaller than in the pH unadjusted runs where only few crystals grew large. Low-concentration sulfuric acid already reduces the lifespan of the transitional colloidal nanophases and the final crystalline Co-struvite significantly. From the point of view of saturation index (SI) and ion activity product (IAP), an initial basic pH increases the $\text{SI}_{\text{M-struvite}}$ as the activity of $[\text{PO}_4^{3-}_{(\text{aq})}]$ increases. However, this shift of the equilibrium to the product side is limited to a certain pH, because at a high pH (for Mg-struvite $\text{pH} = 11$) the presence of $\text{NH}_3^0_{(\text{aq})}$ and $\text{M}(\text{OH})_{(\text{aq})}$ species reduces the activities of $\text{NH}_4^+_{(\text{aq})}$ and M^{2+} and therefore compensates the increase of activity of $\text{PO}_4^{3-}_{(\text{aq})}$ ³⁹.

Phase stability from a point of view of a metal coordination environment

Co-struvite exhibits a low stability compared to Ni-struvite as it decomposes to Co-dittmarite in air or is replaced at higher concentrations of $c(\text{Co}^{2+}) > 0.4$ by CPO as the most stable phase. Hints on these stability properties are hidden in the metal coordination environment. The CoO_6 octahedron in the struvite structure shows a higher degree of distortion compared to NiO_6 in Ni-struvite, but a lower one compared to the other Co-phases (see pre-peak area fits in Table 1). According to that the distortion of the CoO_6 octahedron as well as the configuration of three different bond distances with low degeneracies of two (Figure 7) may not be favorable for the struvite structure. The volume and the distortion of the CoO_6 octahedron could expand the stability of the M-struvite structure and therefore, it tends to decompose to Co-dittmarite. Here, the Co-dittmarite structure allows for a more distorted coordination environment of the central metal cation since it is coordinated by five corner-linking O^{2-} anions of the phosphate tetrahedrons and one O^{2-} anion from the remaining crystal water (SI: Figure S13). This assumption takes into account the high stability of Co(II) phosphate octahydrate at high M/P ratios > 0.4 (see Figure 1 and Figure 4B), where Co^{2+} is also bound in a similar distorted octahedral coordination as in Co-dittmarite (i.e. by two corner

linking O^{2-} anions of the phosphate tetrahedrons and four O^{2-} anions from the crystal water (SI: Figure S13)). As H_2O behaves as a weak-field ligand for most of the bivalent transition metal ions, the high spin configuration is realized in their complexes. Looking at the Irving-Williams thermodynamic series of high spin first row transition metals in the bivalent oxidation state the stability of metal complexes decreases in the order $Mn^{2+} < Fe^{2+} < Co^{2+} < Ni^{2+} < Cu^{2+} > Zn^{2+}$ regardless of the type of coordinated ligands^{42, 43}. Co^{2+} as a d^7 ion shows a strong Jahn-Teller effect in octahedral coordination with weak ligands like H_2O (high-state) compared to Ni^{2+} with a d^8 orbitals as more unpaired electrons occur in this electron configuration. In agreement with our results, other studies demonstrated a distorted non-centrosymmetric octahedral coordination of Co^{2+} as d^7 ion in Co-doped Ni-struvite while Ni^{2+} as a d^8 ion exhibits a near ideal cubic octahedral coordination based on electron spin resonance spectroscopy⁴⁴. Therefore, we suggest that the different stabilities of Ni- and Co-struvite are mainly influenced by the electronical d-configuration and their ionic radii for the struvite structure $Pmn2_1$. We speculate that other 3d ions like Zn^{2+} , Cu^{2+} or Fe^{2+} , which tend to form amorphous and/or other crystalline phases could be potentially precipitated as M-struvite as soon as low amounts of Ni or Co are added. In such a way 3d metals which are favored in the M-struvite structure can stabilize other misfitting 3d metals in the crystal. Since, in wastewaters multiple metal cations are present, an increase in a struvite “fitting” element like Ni could lead to a precipitation of struvite solid solution between all these 3d metals.

Significance of amorphous phases

Interestingly, Mg-struvite and Ni-struvite seem to have a higher stability compared to Co-struvite as no other phases precipitate and no decomposition to other phases could be observed. From dry TEM and cryo-TEM measurements combined with SAED patterns we found no indication or even hint for an amorphous phase in the Mg-system as the crystals grew immediately after mixing to μm size (Figure 3, SI: Figure S4). In contrast, short-lived amorphous nanophases occurred in the Ni-system which form in the early stages of precipitation within seconds. These regular amorphous agglomerates of spherical particles probably aggregate and transform at higher reaction times to a precursor unit of a crystal. The Co-system exhibits metastable long-lived (minutes to hours) amorphous phases on the way to the final crystalline Co-struvite, which is correlated with a color change from purple to light pink. Here, the Co^{2+} changes its configuration from tetrahedral to octahedral coordination which leads to a slightly different color absorption^{34, 35}. Similarly to the Ni-samples, cobalt formed round amorphous nanoparticles (Figure 3, SI: Figure S6). The condensation and densification to a proto-crystalline unit took place throughout a longer time period (mins to hours) than in the Ni-system. This is also reflected in the pH curves at high and low concentrations and the associated color change of the aqueous solution. It may explain why only a weak correlation between concentration of Co^{2+} /DAP and the resulting crystal habit is observed compared to Ni and Mg. Based on the results, it is clear that crystallization of transition metal struvites follows a non-classical nucleation pathway^{45, 46} which involves transitional amorphous precursor phases on the way to the final crystalline product (Figure 8). Here, amorphous colloidal nanoparticles form within seconds, aggregate and transform

within minutes of reaction time. These aggregates transform to a proto-crystalline nucleus which facilitate the next crystallisation of new nuclei. In the final step depending on the reaction conditions these crystal nuclei develop into different morphologies and sizes of crystals.

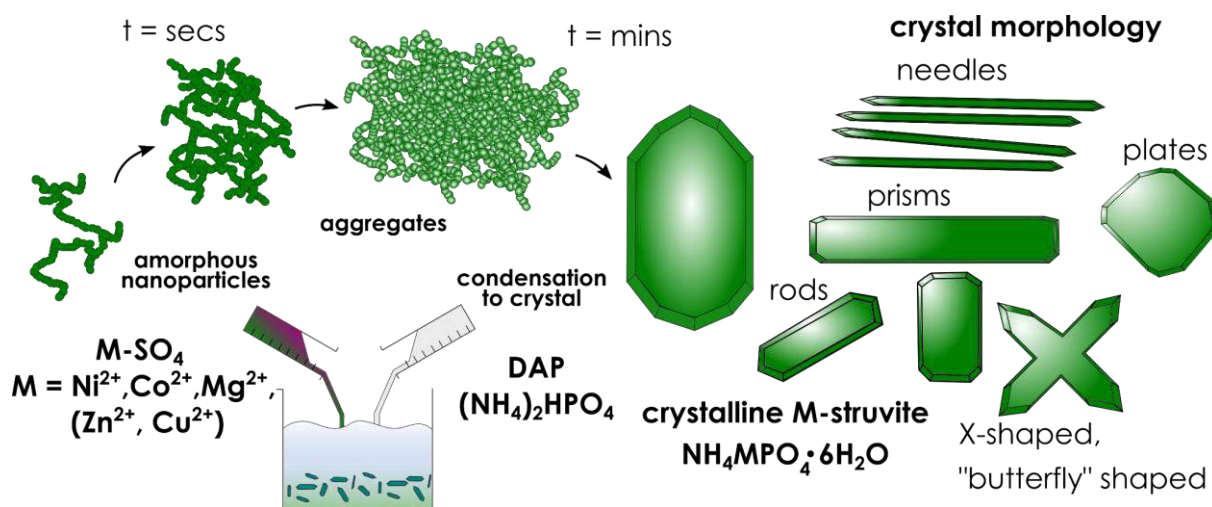


Figure 8: Visualization of the formation of different transition metal struvite crystals through a non-classical crystallization route including amorphous nanoparticles. Stages according to the labels.

Conclusion

Our investigation of transition metal struvites as potential systems for multicomponent precipitation led to several crucial insights. Ni-struvite is stable in multiple concentrations of the reactants and at different metal/phosphate (M/P) ratios. Co-struvite precipitates at a M/P ratio of 0.4, whereas above this value only Co(II)-phosphate octahydrate is stable. Ni- and Co struvites form amorphous precursor phases on the way to the final crystalline product while no nanophase was observed for Mg. Control of different morphologies and sizes of transition metal struvite can be achieved depending on the crystallization conditions. Transition metal phosphates appear to form through non-classical nucleation pathways, which involve multiple amorphous nanophases during precipitation. Due to the low solubility product and their controlled precipitation through adjusting the reaction conditions transition metal struvite is a promising recovery material for extracting NH_4^+ , PO_4^{3-} and transition metals at simultaneously, out of agricultural and mine wastewaters. Furthermore, the possibility to specifically set/tune the morphology and properties opens the prospect of up-cycling materials directly as raw materials for applications (e.g. electrocatalysis).

Acknowledgements

We acknowledge Uwe Reinholz, Martin Radtke and Kirill Yusenko for their support in the XAS measurements at the BAMline beamline of BESSY II. We acknowledge BAM and Helmholtz-Zentrum Berlin (HZB) for providing us with the beamtime at BESSY II. We thank Carsten Prinz for TEM measurements.

References

1. Cordell, D.; Drangert, J.-O.; White, S., The story of phosphorus: Global food security and food for thought. *Global Environmental Change* **2009**, *19*, (2), 292-305.
2. Filippelli, G. M., The Global Phosphorus Cycle. *Reviews in Mineralogy and Geochemistry* **2002**, *48*, (1), 391-425.
3. Gislev, M.; Grohol, M.; Mathieux, F.; Ardente, F. *Report on Critical Raw Materials in the Circular Economy*; European Commission: 2018.
4. Neset, T. S.; Cordell, D., Global phosphorus scarcity: identifying synergies for a sustainable future. *J Sci Food Agric* **2012**, *92*, (1), 2-6.
5. Hallas, J.; Mackowiak, C.; Wilkie, A.; Harris, W., Struvite Phosphorus Recovery from Aerobically Digested Municipal Wastewater. *Sustainability* **2019**, *11*, (2).
6. Prot, T.; Korving, L.; Dugulan, A. I.; Goubitz, K.; van Loosdrecht, M. C. M., Vivianite scaling in wastewater treatment plants: Occurrence, formation mechanisms and mitigation solutions. *Water Res* **2021**, *197*, 117045.
7. Le Corre, K. S.; Valsami-Jones, E.; Hobbs, P.; Parsons, S. A., Phosphorus Recovery from Wastewater by Struvite Crystallization: A Review. *Critical Reviews in Environmental Science and Technology* **2009**, *39*, (6), 433-477.
8. Uysal, A.; Yilmazel, Y. D.; Demirer, G. N., The determination of fertilizer quality of the formed struvite from effluent of a sewage sludge anaerobic digester. *J Hazard Mater* **2010**, *181*, (1-3), 248-54.
9. Hao, X.; Wang, C.; van Loosdrecht, M. C.; Hu, Y., Looking beyond struvite for P-recovery. *Environ Sci Technol* **2013**, *47*, (10), 6-4965.
10. Sena, M.; Seib, M.; Noguera, D. R.; Hicks, A., Environmental impacts of phosphorus recovery through struvite precipitation in wastewater treatment. *Journal of Cleaner Production* **2021**, *280*.
11. Zhao, H.; Yuan, Z. Y., Insights into Transition Metal Phosphate Materials for Efficient Electrocatalysis. *ChemCatChem* **2020**, *12*, (15), 3797-3810.
12. Lin, R.; Ding, Y., A Review on the Synthesis and Applications of Mesoporous Transition Metal Phosphates. *Materials (Basel)* **2013**, *6*, (1), 217-243.
13. Xu, X.; Du, P.; Guo, T.; Zhao, B.; Wang, H.; Huang, M., In situ Grown Ni phosphate@Ni₁₂P₅ Nanorod Arrays as a Unique Core-Shell Architecture: Competitive Bifunctional Electrocatalysts for Urea Electrolysis at Large Current Densities. *ACS Sustainable Chemistry & Engineering* **2020**, *8*, (19), 7463-7471.
14. Meguerdichian, A. G.; Jafari, T.; Shakil, M. R.; Miao, R.; Achola, L. A.; Macharia, J.; Shirazi-Amin, A.; Suib, S. L., Synthesis and Electrocatalytic Activity of Ammonium Nickel Phosphate, [NH₄]NiPO₄·6H₂O, and beta-Nickel Pyrophosphate, beta-Ni₂P₂O₇: Catalysts for Electrocatalytic Decomposition of Urea. *Inorg Chem* **2018**, *57*, (4), 1815-1823.
15. Huang, H.; Xu, C.; Zhang, W., Removal of nutrients from piggery wastewater using struvite precipitation and pyrogenation technology. *Bioresour Technol* **2011**, *102*, (3), 8-2523.
16. El Diwani, G.; El Rafie, S.; El Ibiari, N. N.; El-Aila, H. I., Recovery of ammonia nitrogen from industrial wastewater treatment as struvite slow releasing fertilizer. *Desalination* **2007**, *214*, (1-3), 200-214.
17. Münch, E. V.; Barr, K., Controlled struvite crystallisation for removing phosphorus from anaerobic digester sidestreams. *Water Research* **2001**, *35*, (1), 151-159.
18. Zhangchen, R.; Liu, W. G., Q.; Ji, H.; Li, Y.; Zhang, J.; Song, J.; Zhong, Y.; Zhou, L., Struvite as seed materials for treatment of heavy metals in wastewater. *IOP Conference Series: Earth and Environmental Science (EES)* **2021**, *770*, 1-5.

19. Rouff, A. A., Sorption of chromium with struvite during phosphorus recovery. *Environ Sci Technol* **2012**, *46*, (22), 12493-501.
20. Rouff, A. A.; Juarez, K. M., Zinc interaction with struvite during and after mineral formation. *Environ Sci Technol* **2014**, *48*, (11), 6342-9.
21. Lu, X.; Huang, Z.; Liang, Z.; Li, Z.; Yang, J.; Wang, Y.; Wang, F., Co-precipitation of Cu and Zn in precipitation of struvite. *Sci Total Environ* **2021**, *764*, 144269.
22. Lin, J.; Chen, N.; Pan, Y., Arsenic incorporation in synthetic struvite (NH₄MgPO₄·6H₂O): a synchrotron XAS and single-crystal EPR study. *Environ Sci Technol* **2013**, *47*, (22), 35-12728.
23. Ravikumar, R.; Chandrasekhar, A.; Rama Krishnar, C.; Reddy, Y., X-ray powder diffraction, thermal analysis and IR studies of zinc ammonium phosphate hexahydrate. *Optoelectronics and Advanced Materials -Rapid Communications* **2010**, *4*, 215-219.
24. Abbona, F.; Angela-Frachini, M.; Croni Bono, C.; Lundager Madsen, H., Effect of ammonia excess on the crystal habit of NiNH₄PO₄·6H₂O (Ni-struvite). *Journal of Crystal Growth* **1994**, *143*, 256-260.
25. Haferburg, G.; Kloess, G.; Schmitz, W.; Kothe, E., "Ni-struvite" - a new biomineral formed by a nickel resistant *Streptomyces acidiscabies*. *Chemosphere* **2008**, *72*, (3), 517-23.
26. Hövelmann, J.; Stawski, T. M.; Freeman, H. M.; Besselink, R.; Mayanna, S.; Perez, J. P. H.; Hondow, N. S.; Benning, L. G., Struvite Crystallisation and the Effect of Co²⁺ Ions. *Minerals* **2019**, *9*, (9).
27. Hovelmann, J.; Stawski, T. M.; Besselink, R.; Freeman, H. M.; Dietmann, K. M.; Mayanna, S.; Pauw, B. R.; Benning, L. G., A template-free and low temperature method for the synthesis of mesoporous magnesium phosphate with uniform pore structure and high surface area. *Nanoscale* **2019**, *11*, (14), 6939-6951.
28. Zhao, Y.; Chen, Z.; Xiong, D. B.; Qiao, Y.; Tang, Y.; Gao, F., Hybridized Phosphate with Ultrathin Nanoslices and Single Crystal Microplatelets for High Performance Supercapacitors. *Sci Rep* **2016**, *6*, 17613.
29. Parkhurst, D. L.; Appelo, C. A. J., *Description of input and examples for PHREEQC version 3: a computer program for speciation, batch-reaction, one-dimensional transport, and inverse geochemical calculations*. U.S. Geological Survey: Reston, VA, 2013.
30. Madsen, H. E. L., Solubility Product of Ni-Struvite, NH₄NiPO₄·6H₂O, at 25°C. *Advances in Chemical Engineering and Science* **2017**, *07*, (02), 206-214.
31. Görner, W.; Hentschel, M. P.; Müller, B. R.; Riesemeier, H.; Krumrey, M.; Ulm, G.; Dietsch, W.; Klein, U.; Frahm, R., BAMline: the first hard X-ray beamline at BESSY II. *Nuclear Instruments and Methods in Physics Research A* **2001**, *467-468*, 703-706.
32. Ravel, B.; Newville, M., ATHENA, ARTEMIS, HEPHAESTUS: data analysis for X-ray absorption spectroscopy using IFEFFIT. *J Synchrotron Radiat* **2005**, *12*, (4), 537-41.
33. Momma, K.; Izumi, F., VESTA: a three-dimensional visualization system for electronic and structural analysis. *Journal of Applied Crystallography* **2008**, *41*, (3), 653-658.
34. Bach, S.; Visnow, E.; Panthöfer, M.; Gorelik, T.; Buzanich, A. G.; Gurlo, A.; Kolb, U.; Emmerling, F.; Lind, C.; Tremel, W., Hydrate Networks under Mechanical Stress - A Case Study for Co₃(PO₄)₂·8H₂O. *European Journal of Inorganic Chemistry* **2016**, *2016*, (13-14), 2072-2081.
35. Bach, S.; Panthöfer, M.; Bienert, R.; Buzanich, A. G.; Emmerling, F.; Tremel, W., Role of Water During Crystallization of Amorphous Cobalt Phosphate Nanoparticles. *Crystal Growth & Design* **2016**, *16*, (8), 4232-4239.

36. Crutchik, D.; Garrido, J. M., Struvite crystallization versus amorphous magnesium and calcium phosphate precipitation during the treatment of a saline industrial wastewater. *Water Sci Technol* **2011**, *64*, (12), 7-2460.
37. Zhang, Q.; Jiang, Y.; Gou, B.-D.; Huang, J.; Gao, Y.-X.; Zhao, J.-T.; Zheng, L.; Zhao, Y.-D.; Zhang, T.-L.; Wang, K., In Situ Detection of Calcium Phosphate Clusters in Solution and Wet Amorphous Phase by Synchrotron X-ray Absorption Near-Edge Spectroscopy at Calcium K-Edge. *Crystal Growth & Design* **2015**, *15*, (5), 2204-2210.
38. Mahamid, J.; Sharir, A.; Weiner, S., Amorphous calcium phosphate is a major component of the forming fin bones of zebrafish: Indications for an amorphous precursor phase. *PNAS* **2008**, *105*, 12748-12753.
39. Shaddel, S.; Ucar, S.; Andreassen, J. P.; Osterhus, S. W., Enhancing efficiency and economics of phosphorus recovery process by customizing the product based on sidestream characteristics - an alternative phosphorus recovery strategy. *Water Sci Technol* **2019**, *79*, (9), 1777-1789.
40. Blyholder, G.; Ford, N., Far-Infrared Spectra of some Mono- and Polynuclear Aqua-Substituted cobalt-Ammine Complexes. *The Journal of Physical Chemistry* **1964**, *68*, (6), 1496-1500.
41. Schmiedekamp, A. M.; Ryan, M. D.; Deeth, R. J., Six-Coordinate Co^{2+} with H_2O and NH_3 Ligands: Which Spin State Is More Stable? *Inorganic Chemistry* **2002**, *41*, 5733-5743.
42. Irving, H.; Williams, R., Order of stability of metal complexes. *Nature* **1948**, *162*.
43. Irving, H.; Williams, R., The stability of transition-metal complexes. *J. Chem. Soc.* **1953**, 3192-3210.
44. Foglio, M. B., G., Study of Co^{2+} in Different Crystal Field Environments. *Brazilian Journal of Physics* **2005**, *36*, 40-54.
45. De Yoreo, J., Crystal nucleation: more than one pathway. *Nat Mater* **2013**, *12*, (4), 5-284.
46. Andreassen, J.-P.; Lewis, A. E., Classical and Nonclassical Theories of Crystal Growth. In *New Perspectives on Mineral Nucleation and Growth*, 2017; pp 137-154.

Supporting Information for:

Ni- and Co-struvites: Revealing crystallization mechanisms and crystal engineering for phosphorous and transition metal recovery

Stephanos Karafiludis^{1*}, Ana Guilherme Buzanich¹, Zdravko Kochovski², Ines Feldmann¹, Franziska Emmerling^{1,3}, and Tomasz M. Stawski^{1**}

¹Federal Institute for Materials Research and Testing, Richard-Willstätter-Straße 11, 12489 Berlin, Germany;

²Department for Electrochemical Energy Storage, Helmholtz-Zentrum Berlin for Materials and Energy, Hahn-Meitner Platz 1, 14109 Berlin, Germany;

³Department of Chemistry, Humboldt-Universität zu Berlin, Brook-Taylor-Straße 2, 12489 Berlin

Corresponding authors: **tomasz.stawski@bam.de; *stephanos.karafiludis@bam.de

List of Tables

Table S1: Detailed reaction conditions for the precipitated samples.....	2
Table S2: PHREEQC calculations of pH change in the solution	3
Table S3: ARTEMIS fit parameter for Ni-struvite R-factor= 0.005.....	4
Table S4: ARTEMIS fit parameter for Co-struvite R-factor= 0.012.....	5
Table S5: ARTEMIS fit parameter for Co-dittmarite (COD), R-factor= 0.008.....	6
Table S6: ARTEMIS fit parameter for Co-phosphate octahydrate (CPO), R-factor= 0.005.....	7
Table S7: Concentrations of Co, Ni, NH ₄ ⁺ and PO ₄ ³⁻ /total phosphorus in different wastewaters.....	8

List of Figures

Figure S1: XRD patterns of Mg, Ni and Co phosphates	9
Figure S2: Additional XRD patterns of Co phosphates	10
Figure S3: XRD patterns of pH adjusted samples.....	11
Figure S4: Conventional TEM images of the Mg sample.....	12
Figure S5: Conventional STEM analysis of Ni sample after t = 5 sec mixing.....	13
Figure S6: Conventional STEM analysis of Co sample after t = 5 sec mixing.....	14
Figure S7: SEM images of Ni-struvite	15
Figure S8: SEM images of pH adjusted Ni samples	16
Figure S9: SEM images of Co phosphate images.....	17
Figure S10: SEM images of pH adjusted Co samples.....	18
Figure S11: Crystallization trends in the Ni and Co system.....	19
Figure S12: SEM images of Mg-struvite	20
Figure S13: Crystallographic differences between the Co phosphate phases	21
Supplementary Note:	22
References SI.....	23

Table S1: Detailed reaction conditions for the precipitated samples.

c(NiSO₄)	c(DAP)	M/P ratio	c(CoSO₄)	c(DAP)	M/P ratio	c(MgCl₂)	c(DAP)	M/P ratio
[M]	[M]		[M]	[M]		[M]	[M]	
0.004	0.02	0.2	0.004	0.02	0.2	0.004	0.02	0.2
0.01	0.05	0.2	0.008	0.02	0.4	0.01	0.05	0.2
0.012	0.02	0.6	0.01	0.05	0.2	0.012	0.02	0.6
0.02	0.02	1	0.012	0.02	0.6	0.02	0.02	1
0.02	0.1	0.2	0.02	0.02	1	0.02	0.1	0.2
0.03	0.05	0.6	0.02	0.1	0.2	0.03	0.05	0.6
0.04	0.1	0.4	0.03	0.05	0.6	0.04	0.1	0.4
0.05	0.05	1	0.04	0.1	0.4	0.05	0.05	1
0.06	0.1	0.6	0.042	0.1	0.42	0.06	0.1	0.6
0.08	0.1	0.8	0.046	0.1	0.46	0.08	0.1	0.8
0.1	0.1	1	0.05	0.05	1	0.1	0.1	1
0.15	0.1	1.5	0.05	0.1	0.5	0.15	0.1	1.5
0.3	0.1	3	0.054	0.1	0.54	0.3	0.1	3
			0.058	0.1	0.58			
			0.06	0.1	0.6			
			0.08	0.1	0.8			
			0.1	0.1	1			
			0.15	0.1	1.5			
			0.3	0.1	3			

Table S2: PHREEQC calculations of pH changes in solution with 100 ml 0.1 M DAP and 100 ml of 0.02 M M^{2+} (M = Mg, Co, Ni) with different amounts of 1 M $NaOH_{(aq)}$ (pH = 13.97) and 0.1 M $H_2SO_{4(aq)}$ (pH = 1.00).

Experimental conditions		M/P ratio = 0.2		c(MSO ₄) [mM] = 20		c(DAP) [mM] = 100	
Sample with normal pH	amount of 1M $NaOH_{(aq)}$ [ml]	calculated pH _{eq}	ΔpH	amount of 0.1M $H_2SO_{4(aq)}$ [ml]	calculated pH _{eq}	ΔpH	
Ni-struvite pH _{eq} = 6.87	1	7.03	0.16	1	6.82	-0.05	
	2	7.21	0.33	2	6.78	-0.10	
	3	7.40	0.53	3	6.73	-0.15	
	4	7.66	0.78	4	6.68	-0.20	
	5	8.04	1.17	5	6.63	-0.25	
	6	8.47	1.60	6	6.57	-0.30	
	7	8.78	1.90	7	6.52	-0.35	
	8	8.99	2.12	8	6.46	-0.42	
	9	9.17	2.30	9	6.41	-0.47	
	10	9.32	2.45	10	6.35	-0.53	
Co-struvite pH _{eq} = 7.02	1	7.18	0.16	1	6.98	-0.04	
	2	7.37	0.35	2	6.94	-0.08	
	3	7.60	0.58	3	6.90	-0.12	
	4	7.89	0.87	4	6.86	-0.16	
	5	8.19	1.17	5	6.83	-0.19	
	6	8.38	1.36	6	6.79	-0.23	
	7	8.51	1.49	7	6.76	-0.26	
	8	8.59	1.57	8	6.72	-0.30	
	9	8.66	1.64	9	6.67	-0.35	
	10	8.75	1.73	10	6.61	-0.41	
Mg-struvite pH _{eq} = 7.33	5	8.86	1.84	5	6.99	-0.03	
	10	9.45	2.43	10	6.71	-0.62	

Table S3: ARTEMIS fit parameter for Ni-struvite R-factor= 0.005.

sample	scattering path	degeneracy	σ^2	$R_{\text{diff}} [\text{\AA}]$	$R_{\text{diff}}^2 [\text{\AA}^2]$	$R_{\text{model}} [\text{\AA}]$	$R_{\text{fit}} [\text{\AA}]$
Ni-struvite	Ni1-O1	4	0.009	-0.001	1.00E-06	2.046	2.044
NH₄NiPO₄•6H₂O	Ni1-O2	2	0.009	-0.001	1.00E-06	2.089	2.088
mean R_{fit} (err) [\AA]	Ni1-O3 H1	4	-0.001	-0.207	4.29E-02	2.560	2.353
2.059(6)	Ni1-H2	5	0.012	-0.217	4.70E-02	2.586	2.369
V_{sphere} (err) [\AA^3]	Ni1-H3	2	0.012	-0.217	4.70E-02	2.627	2.410
36.6 (2)	Ni1-H4	2	0.012	-0.217	4.70E-02	2.668	2.451
R-factor	Ni1-O1-O1	6	-0.001	-0.207	4.29E-02	3.465	3.258
0.005	Ni1-O3-O2	16	-0.001	-0.207	4.29E-02	3.530	3.322
S_0^2 Amplitude reduction factor (err)	Ni1-N1	1	0.005	-0.186	3.47E-02	4.022	3.836
1.3(1)	Ni1-N2	2	0.005	-0.186	3.47E-02	4.111	3.925
ΔE	Ni1-O4	4	0.006	0.242	5.85E-02	4.084	4.326
3.1(6)	Ni1-O5	2	0.006	0.242	5.85E-02	4.162	4.404
	Ni1-O6	2	0.006	0.242	5.85E-02	4.200	4.442
	Ni1-O7	3	0.006	0.242	5.85E-02	4.272	4.514
	Ni1-O8	2	0.006	0.242	5.85E-02	4.329	4.571

Table S4: ARTEMIS fit parameter for Co-struvite R-factor= 0.012.

sample	scattering path	degeneracy	σ^2	$R_{\text{diff}} [\text{\AA}]$	$R_{\text{diff}}^2 [\text{\AA}^2]$	$R_{\text{model}} [\text{\AA}]$	$R_{\text{fit}} [\text{\AA}]$
Co-struvite	Co1-O1	2	0.005	0.0001	1.69E-08	2.058	2.058
NH₄CoPO₄•6H₂O	Co1-O2	2	0.005	0.0001	1.69E-08	2.089	2.089
mean R_{fit} (err) [\AA]	Co1-O3	2	0.005	0.0001	1.69E-08	2.129	2.129
2.091(1)	Co1-H1	2	0.003	0.3078	9.48E-02	2.211	2.519
V_{sphere} (err) [\AA^3]	Co1-H2	2	0.003	0.3078	9.48E-02	2.451	2.759
38.35(2)	Co1-H3	4	0.003	0.3078	9.48E-02	2.549	2.857
R-factor	Co1-H4	2	0.003	0.3078	9.48E-02	2.616	2.924
0.012	Co1-O1-H3-O1	4	0.003	0.3774	1.42E-01	2.752	3.129
S_{O}^2 Amplitude reduction factor (err)	Co1-O5-O6-O5	2	0.003	0.3774	1.42E-01	2.840	3.217
0.85(5)	Co1-O3-H5-O3	1	0.003	0.3774	1.42E-01	2.843	3.220
ΔE	Co1-O1-O2	6	-0.003	0.2301	5.29E-02	3.507	3.737
4.5(6)	Co1-O1-O3	12	-0.003	0.2301	5.29E-02	3.575	3.805
	Co1-O2-O3	4	-0.003	0.2301	5.29E-02	3.622	3.852
	Co1-N1	1	0.001	-0.0171	2.94E-04	4.027	4.009
	Co1-N2	2	0.001	-0.0171	2.94E-04	4.133	4.115
	Co1-O4	4	0.003	0.3774	1.42E-01	4.105	4.482
	Co1-O6	4	0.003	0.3774	1.42E-01	4.199	4.576
	Co1-O7	3	0.003	0.3774	1.42E-01	4.288	4.665
	Co1-O8	2	0.003	0.3774	1.42E-01	4.362	4.739
	Co1-P1	2	0.003	0.3774	1.42E-01	4.393	4.770

Table S5: ARTEMIS fit parameter for Co-dittmarite (COD), R-factor= 0.008.

sample	scattering path	degeneracy	σ^2	R_{diff} [Å]	R_{diff}^2 [Å ²]	R_{model} [Å]	R_{fit} [Å]
Co-dittmarite	Co1-O1	3	0.001	0.0001	1.69E-08	2.055	2.023
NH ₄ CoPO ₄ •H ₂ O	Co1-O2	3	0.001	0.0001	1.69E-08	2.201	2.169
mean R_{fit} (err) [Å]	Co1-H1	2	-0.008	0.0001	1.69E-08	2.492	2.222
2.096(1)	Co1-H2	2	-0.008	0.3078	9.48E-02	2.970	2.699
V_{sphere} (err)[Å ³]	Co1-P1	1	0.002	0.3078	9.48E-02	2.797	2.797
38.55(2)	Co1-P2	2	0.002	0.3078	9.48E-02	3.209	3.209
R-factor	Co1-O3	2	0.001	0.2301	5.29E-02	3.313	3.281
0.008	Co1-P3	1	0.002	0.3078	9.48E-02	3.305	3.305
S _O ² Amplitude reduction factor	Co1-O4	2	0.001	-0.0171	2.94E-04	3.592	3.560
0.79(6)	Co1-Co2	7	0.010	0.3774	1.42E-01	3.712	3.653
ΔE	Co1-O5	1	0.001	-0.0171	2.94E-04	3.753	3.721
2.6(6)	Co1-N1	1	-0.008	0.3774	1.42E-01	4.010	3.740
	Co1-O6	3	0.001	0.2301	5.29E-02	3.813	3.781
	Co1-O7	1	0.001	0.2301	5.29E-02	3.944	3.912

Table S6: ARTEMIS fit parameter for Co-phosphate octahydrate (CPO), R-factor= 0.005.

sample	scattering path	degeneracy	σ^2	$R_{\text{diff}} [\text{\AA}]$	$R_{\text{diff}}^2 [\text{\AA}^2]$	$R_{\text{model}} [\text{\AA}]$	$R_{\text{fit}} [\text{\AA}]$
Co-octahydrate	Co1-O1	5	0.011	-0.003	8.53E-06	2.021	2.099
Co₃(PO₄)₂•8H₂O	Co1-O2	1	0.011	-0.003	8.53E-06	2.158	2.155
mean R_{fit} (err) [\AA]	Co1-H1	16	0.018	-0.079	6.19E-03	2.451	2.372
2.11(2)	Co1-O2-H2	8	0.001	0.416	1.73E-01	2.593	2.593
V_{sphere} (err)[\AA^3]	Co1-H3	4	0.018	-0.079	6.19E-03	3.226	3.147
39.3(6)	Co1-P1	2	0.010	-0.003	9.18E-06	3.194	3.191
R-factor	Co1-H3	8	0.018	-0.079	6.19E-03	3.319	3.240
0.005	Co1-O3	4	0.001	0.416	1.73E-01	3.579	3.389
S_{O}^2 Amplitude reduction factor (err)	Co1-O1-O2	8	-0.013	0.099	9.82E-03	3.553	3.553
1.3(1)	Co1-O5	2	0.010	-0.003	9.18E-06	3.675	3.576
ΔE	Co1-O1-O2	8	-0.013	0.099	9.82E-03	3.584	3.584
4.9(7)	Co1-O2-O2	8	0.010	-0.003	9.18E-06	3.684	3.672
	Co1-O1-P1	4	-0.013	0.099	9.82E-03	3.389	3.684
	Co1-O4	8	0.010	-0.003	9.18E-06	3.950	3.947
	Co1-H3-O4	16	0.001	0.416	1.73E-01	4.014	4.014
	Co1-O6-H5	8	0.001	0.416	1.73E-01	4.450	4.450

Table S7: Concentrations of Co, Ni, ammonia NH_4^+ and phosphate PO_4^{3-} /total phosphorus (TP) in different wastewaters in mg/L, otherwise unit displayed; agricultural wastewaters contain high amounts of ammonia and phosphorus while mine wastewaters exhibit high concentrations of heavy metals.

country	region	waste water	species	concentration	reference
DRC	Katanga province	mine wastewater	Co	3.164	Atibu et al.2013 ¹
Italy	Rio Piscinas	ground water (contaminated)	Co	2.9-1.5	Concas et al. 2006 ²
			Ni	4.6-3.0	
Turkey	Amik plain	agricultural wastewater	NH_4^+	13	Agca et al. 2014 ³
			TP	87	
			Co	13 [$\mu\text{g/L}$]	
			Ni	50 [$\mu\text{g/L}$]	
USA	Duluth gabbro, Minnesota	mine wastewater	Co	9.8	Hammack et al. 1991 ⁴
			Ni	198	
Jordan	Eshidiya mine	mine wastewater	NH_4^+	95-30[$\mu\text{g/L}$]	Al-Hwaiti et al. 2016 ⁵
			PO_4^{3-}	8.9-0.1	
		ground water	NH_4^+	3.8-3.5	Al-Hwaiti et al. 2016 ⁵
			PO_4^{3-}	50-10 [$\mu\text{g/L}$]	
Zambia	Kabwe	mine wastewater	Co	34,400	Sracek et al. .2010 ⁶
China	Sichuan	agricultural wastewater	NH_4^+	1257.14	Feng et al. 2020 ⁷
			PO_4^{3-}	25.01	
Brazil		agricultural wastewater	NH_4^+	77	Leite et al. 2009 ⁸
			TP	12	
USA	Cobalt, Ontario	surface water	Co	2028-0.5 [$\mu\text{g/L}$]	Percival et al. 1996 ⁹
			Ni	660-2.6 [$\mu\text{g/L}$]	
Serbia	Bor	mine wastewater	Ni	6128	Stopic et al. 2007 ¹⁰
			Co	1.2	

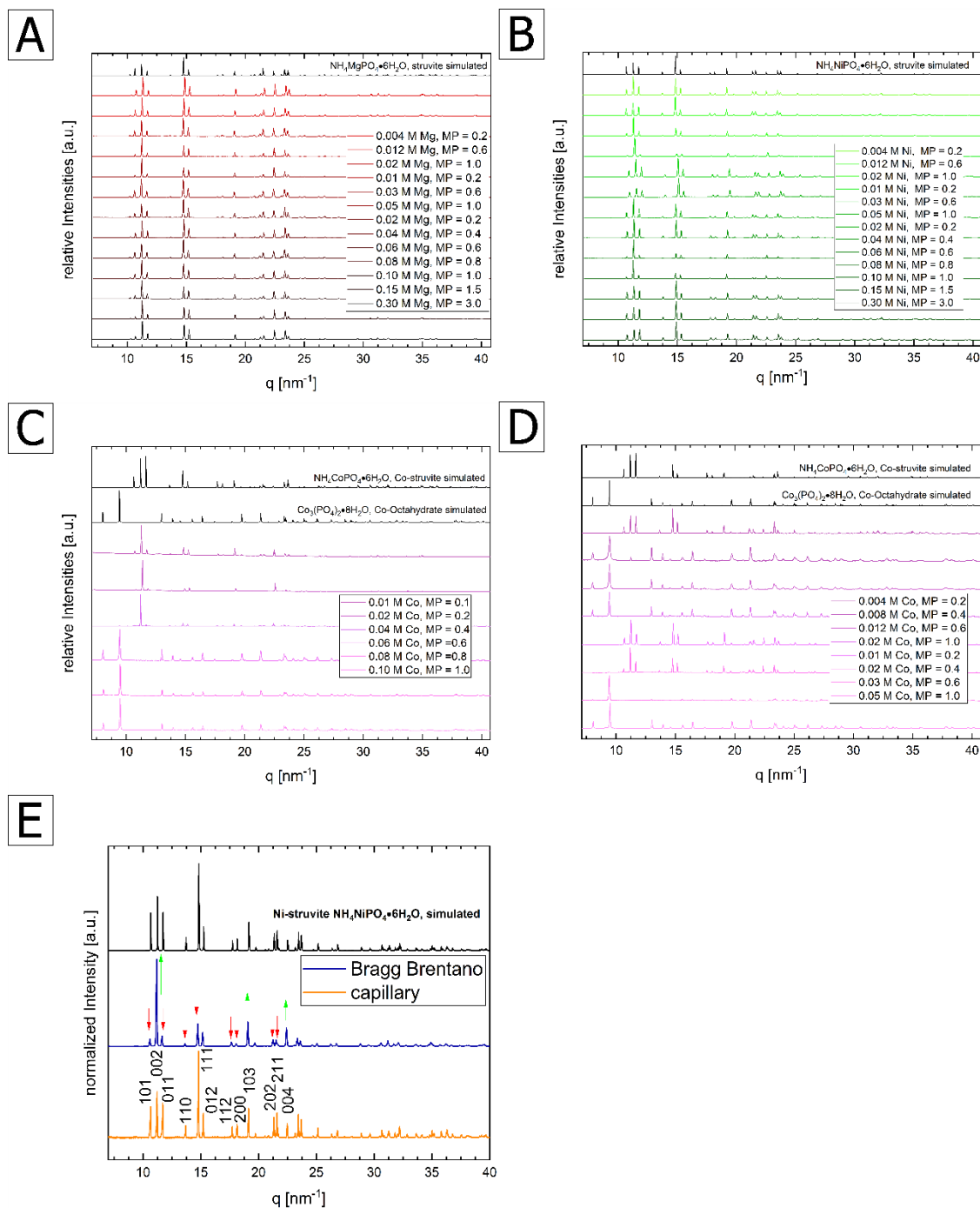


Figure S1: Stacked XRD patterns with the simulated pattern of the phosphate compound in black; (A) Mg-series; (B) Ni-series; (C) and (D) Co-series for different concentrations, according to the legends; These XRD patterns were used to create the phase stability diagrams; Mg-struvite reference COD 9007674; Ni-struvite reference ICSD 403058; Co-struvite reference ICSD 170042; Co(II) phosphate octahydrate reference COD 2020362; (E) In all measured XRD patterns of M-struvite preferred orientation of the (001) crystal planes occurred to a varying degree, and was visible through strong intensity discrepancies between the simulated and measured patterns. All crystal planes with high (h00) or (0k0) component exhibit lower intensities while reflexes with a dominant (00l) component are intensified than in the simulated pattern visible in (E). The preferred orientation is caused by the alignment of elongated habit of the crystals during the preparation of the flat powder sample holders.

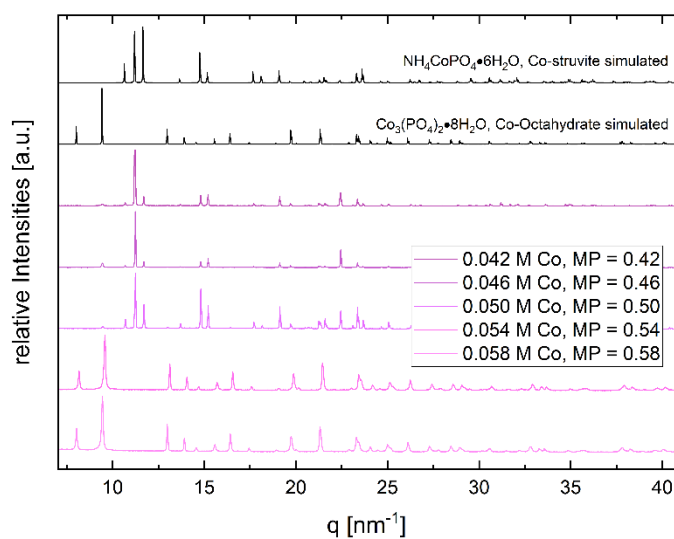
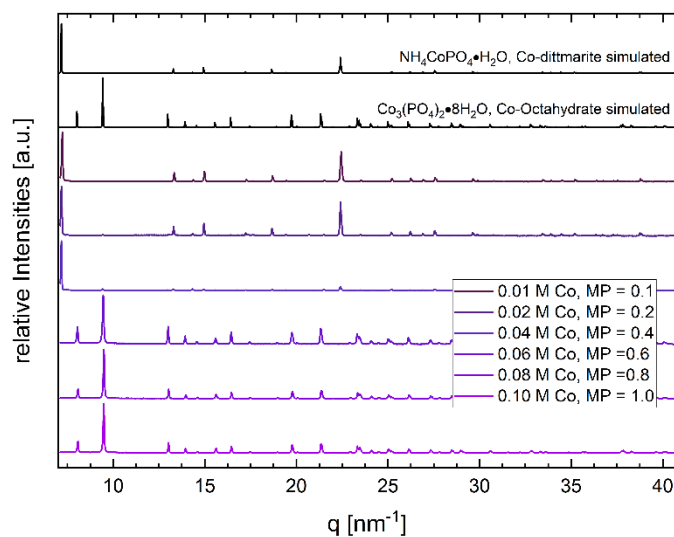
A**B**

Figure S2: Stacked XRD patterns with the simulated pattern of the phosphate compound in black; (A) In the transition interval between M/P ratios of 0.58-0.42 with 0.1 M DAP of the Co-system Co-struvite and Co(II) phosphate octahydrate are stable; (B) Co-struvite decomposes in air to Co-dittmarite, while Co(II)phosphate octahydrate remains stable under these conditions. The same simulated patterns used as in Figure S1 with added Co-dittmarite COD 2008122.

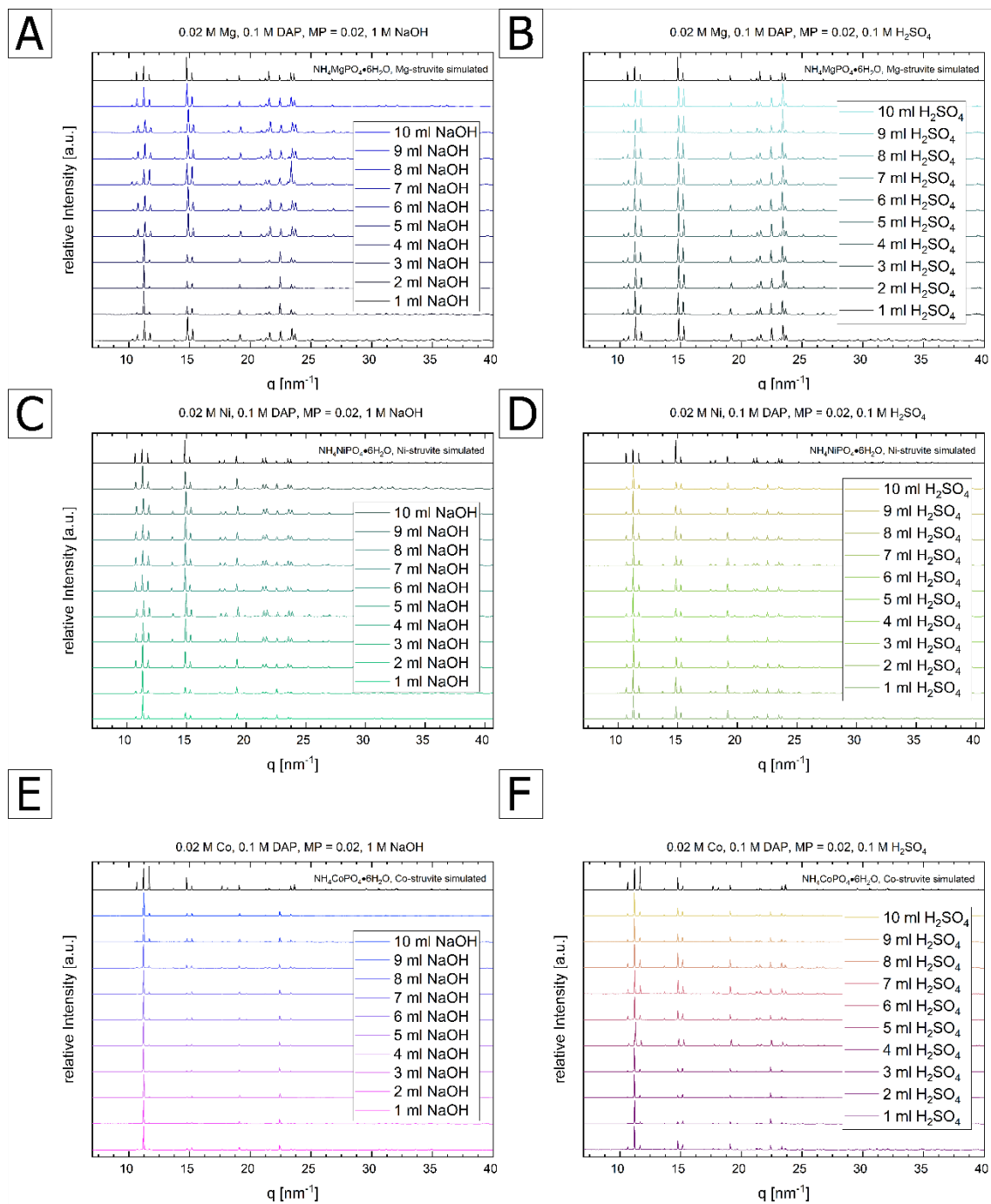


Figure S3: pH adjusted samples with $\text{NaOH}_{(\text{aq})}$ and $\text{H}_2\text{SO}_{4(\text{aq})}$ of (A) (B) Mg; of (C) (D) Ni and (E) (F) Co with their respective experimental conditions (see legends) and their phase composition. In all samples single phase M-struvite precipitated; same simulated patterns used as in Figure S1.

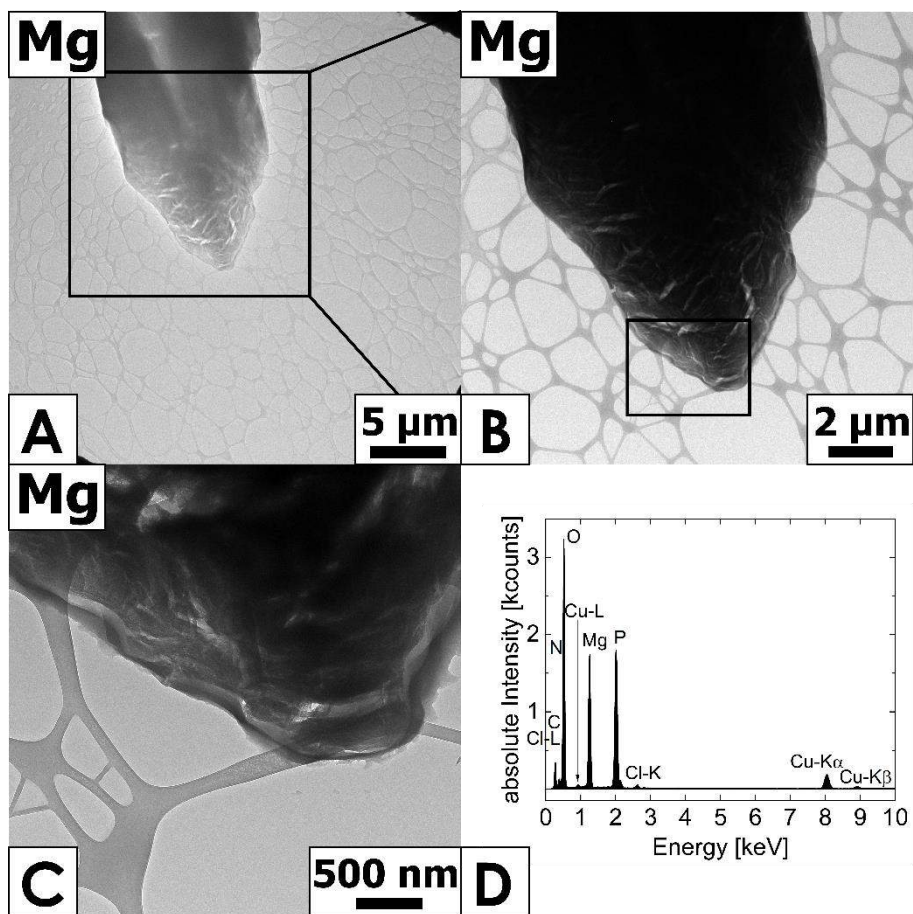


Figure S4: (A) Dry TEM images of Mg sample after 5 seconds mixing forming crystals of μm -size with visible vacuum cracks; (B) detail view of Mg-struvite crystal from the area marked with a black rectangle in (A); (C) close view of the Mg-struvite crystal from the area marked with a black rectangle in (B); (D) EDX spectrum of Mg-struvite.

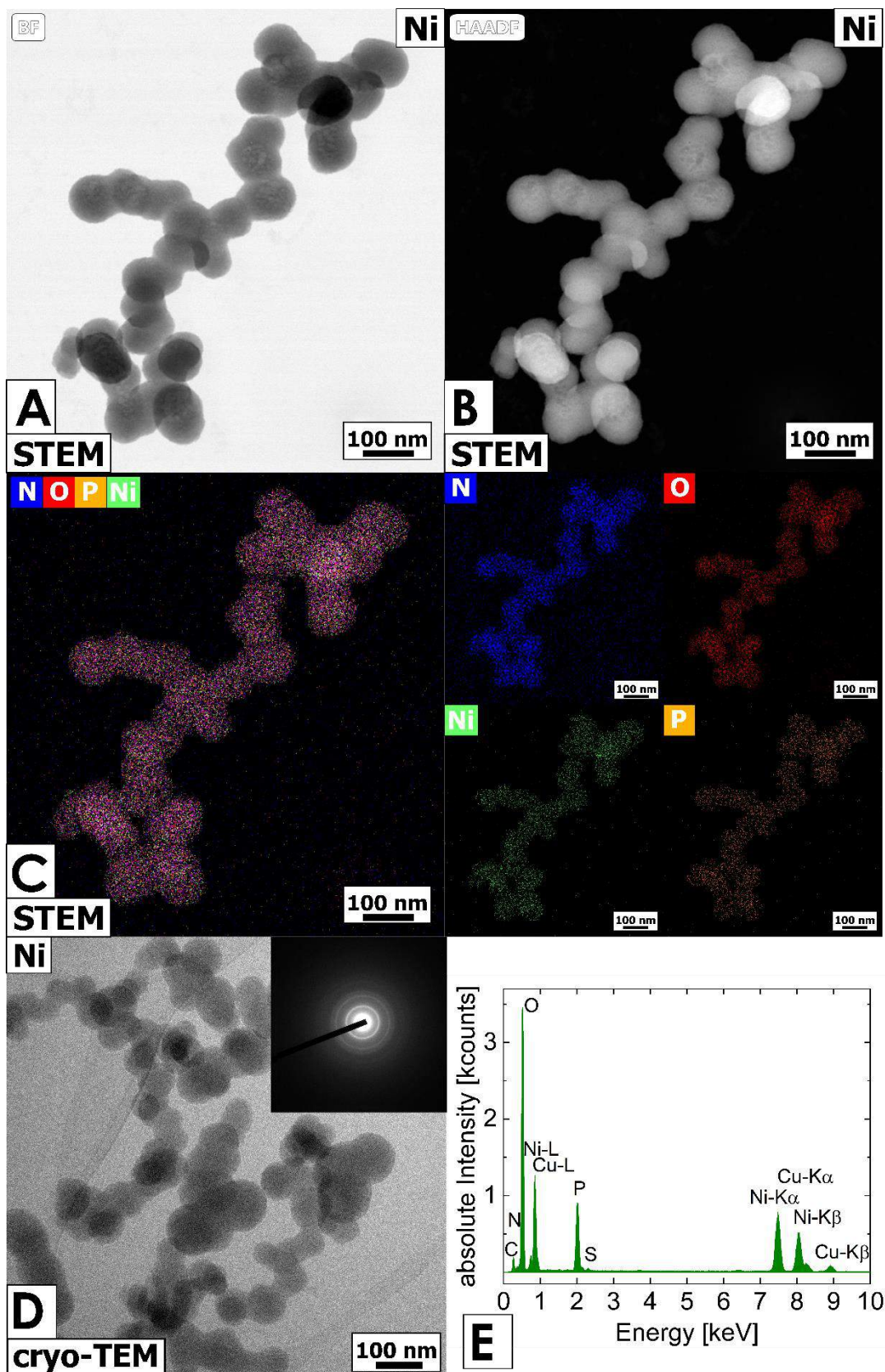


Figure S5: (A) Dry STEM analysis of Ni sample after $t = 5$ sec mixing with the formation of amorphous nanophases in bright field = BF; (B) high angular dark field = HAADF; (C) and elemental mappings of N = nitrogen, O = oxygen, Ni = nickel and P = phosphorus; (D) cryo-TEM image of amorphous Ni-phase with the SAED pattern in the inset; (E) EDX point measurement from amorphous particles.

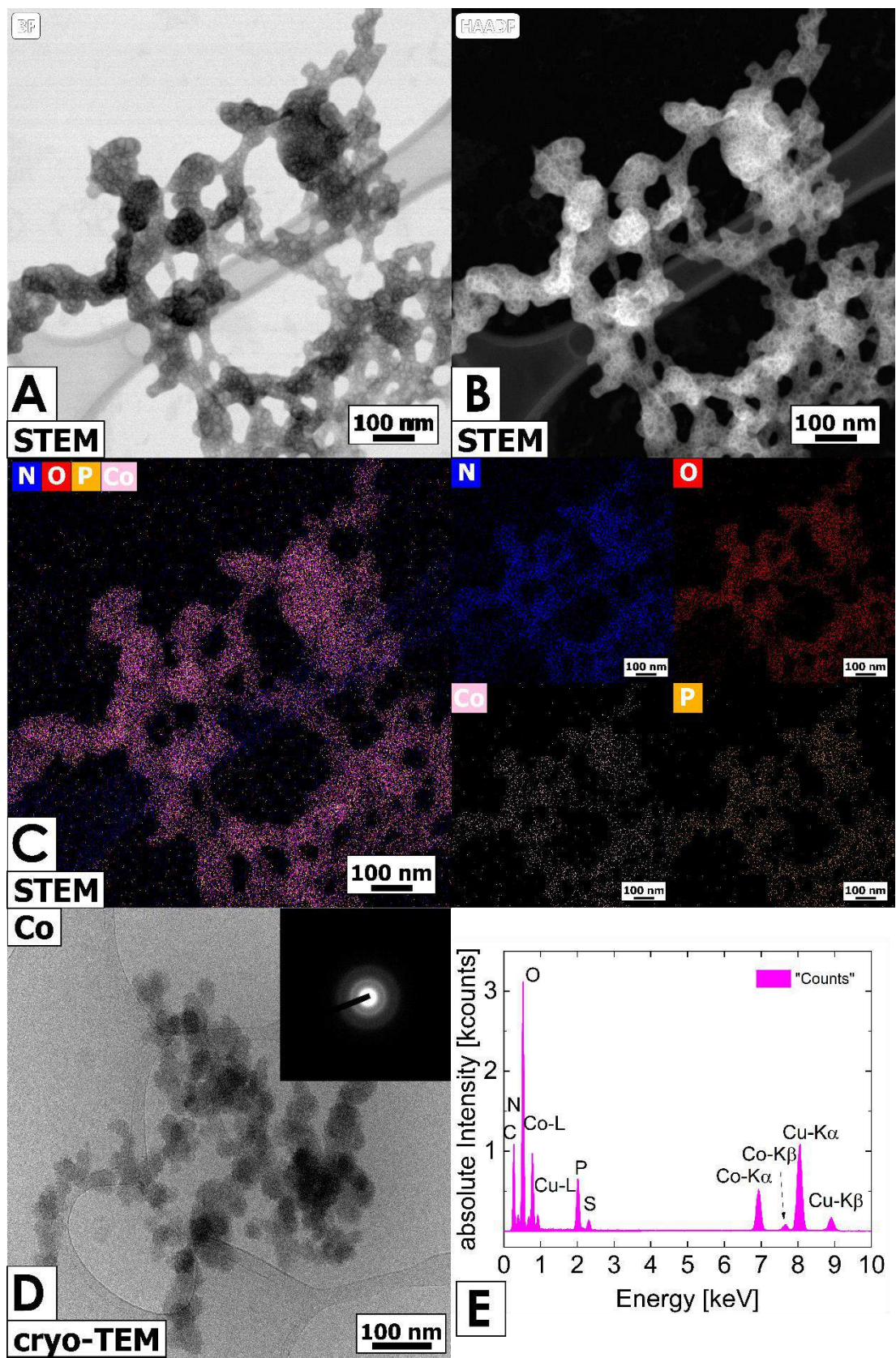


Figure S6: (A) Dry STEM analysis of Co sample after $t = 5$ sec mixing; formation of amorphous nanoparticles in bright field = BF; (B) high angular dark field = HAADF; (C) elemental mappings of N = nitrogen, O = oxygen, Co = cobalt and P = phosphorus; (D) cryo-TEM image of amorphous Co-phase with the SAED pattern; (E) EDX point measurement of amorphous particles.

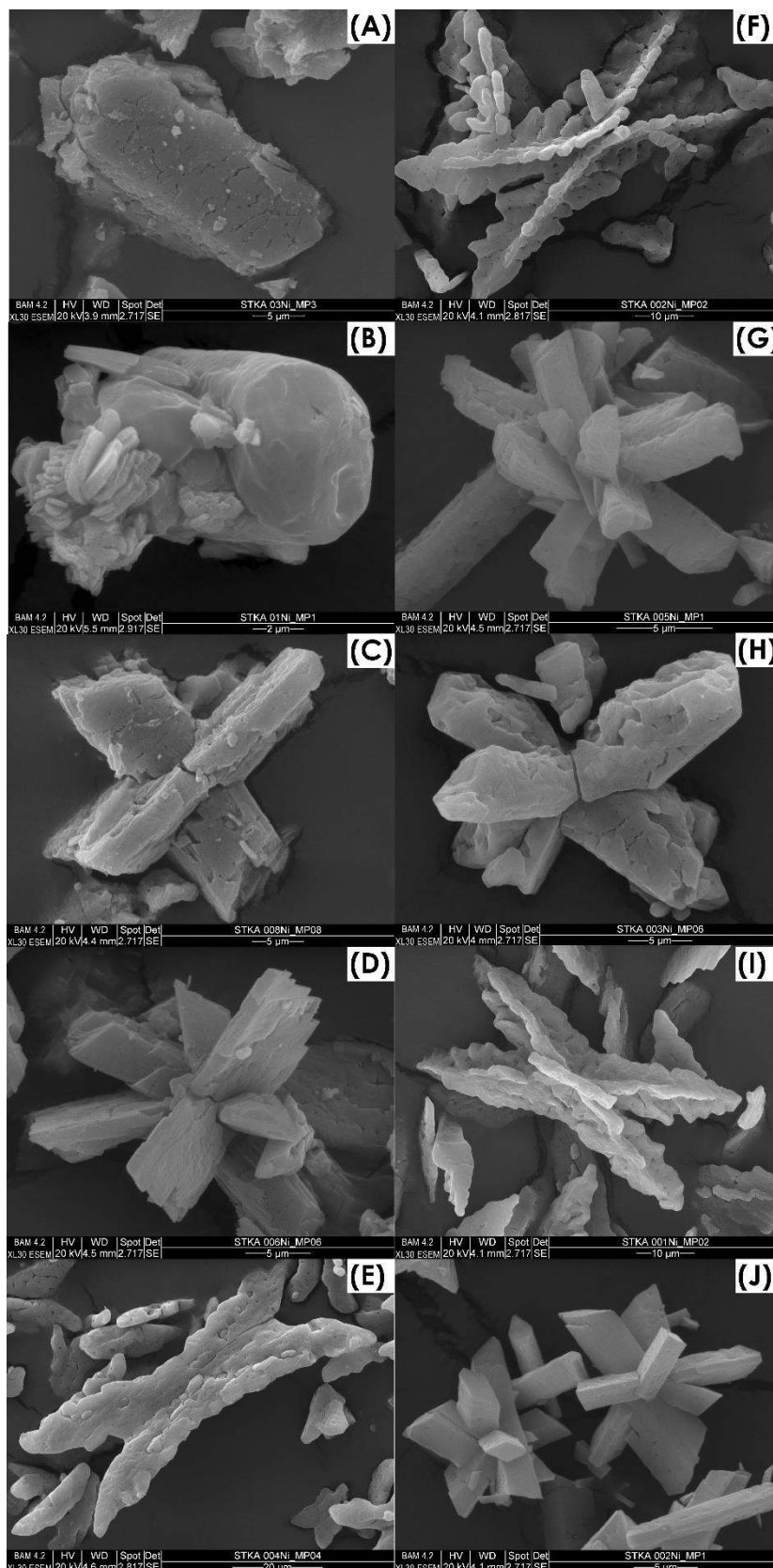


Figure S7: Ni-struvite synthesized at varying concentrations of educts. (A) 0.3 M Ni, 0.1 M DAP, M/P ratio = 3; (B) 0.1 M Ni, 0.1 M DAP, M/P ratio = 1; (C) 0.08 M Ni, 0.1 M DAP, M/P ratio = 0.8; (D) 0.06 M Ni, 0.1 M DAP, M/P ratio = 0.6; (E) 0.04 M Ni, 0.1M DAP, M/P ratio = 0.4; (F) 0.02 M Ni, 0.1 M DAP, M/P ratio = 0.2; (G) 0.05 M Ni, 0.05 M DAP, M/P ratio = 1.0; (H) 0.03 M Ni, 0.05 M DAP, M/P ratio = 0.6; (I) 0.01 M Ni, 0.05M DAP, M/P ratio = 0.2; (J) 0.02 M Ni, 0.02 M DAP, M/P ratio = 1.0.

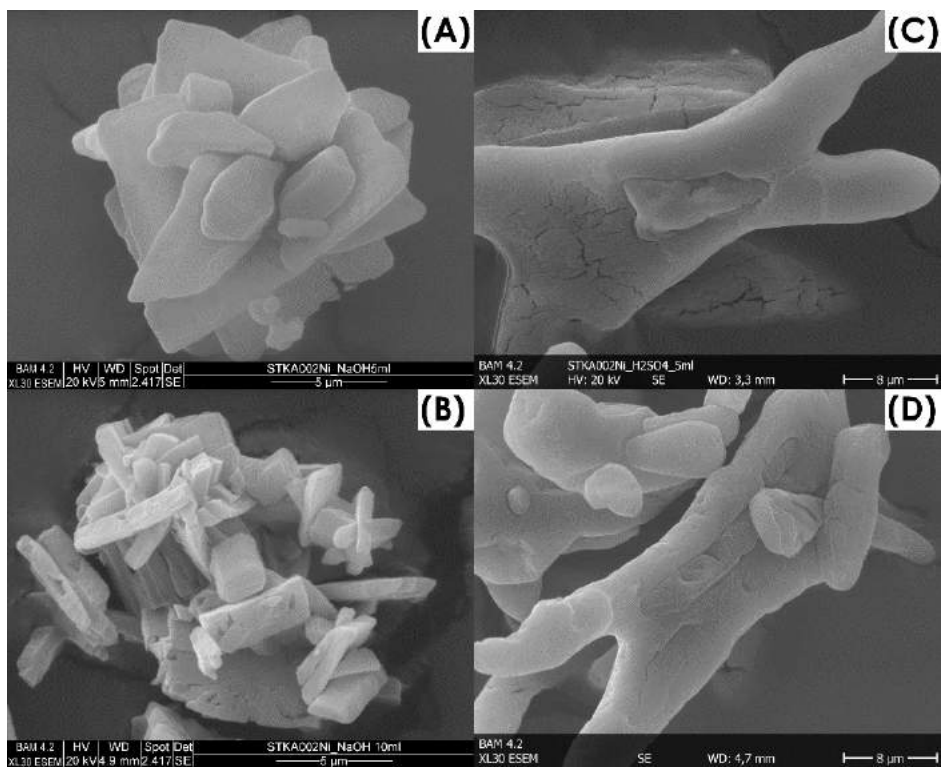


Figure S8: Ni-struvite synthesized from 0.02 M Ni and 0.1 M DAP leading to a M/P ratio of 0.2 at different initial pH with 5 ml and 10 ml 1 M NaOH_(aq) or 0.1 M H₂SO_{4(aq)}; (A) 5 ml 1 M NaOH_(aq); (B) 10 ml 1 M NaOH_(aq); (C) 5 ml 1 M H₂SO_{4(aq)}; (D) 10 ml 1 M H₂SO_{4(aq)}.

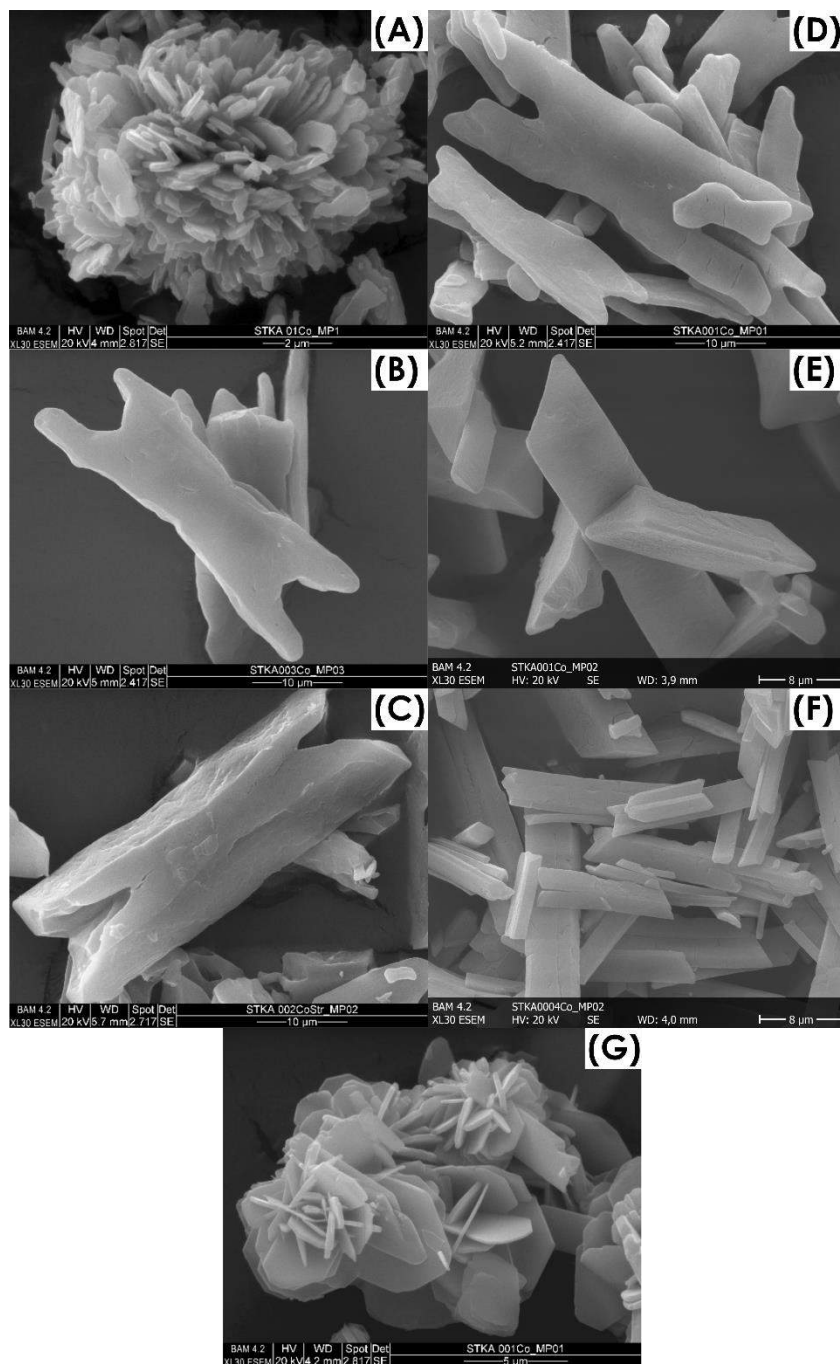


Figure S9: Co-phosphates synthesized at different concentrations. (A) Co(II)phosphate octahydrate 0.1 M Co, 0.1 M DAP, M/P ratio = 1; (B) 0.03 M Co, 0.1 M DAP, M/P ratio = 0.3; (C) 0.02 M Co, 0.1 M DAP, M/P ratio = 0.2; (D) 0.01 M Co, 0.1 M DAP, M/P ratio = 0.1; (E) 0.01 M Co, 0.05 M DAP, M/P ratio = 0.2; (F) 0.004 M Co, 0.02 M DAP, M/P ratio = 0.2; (G) Co-dittmarite in air decomposed 0.01 M Co, 0.1 M DAP, M/P ratio = 1.0.

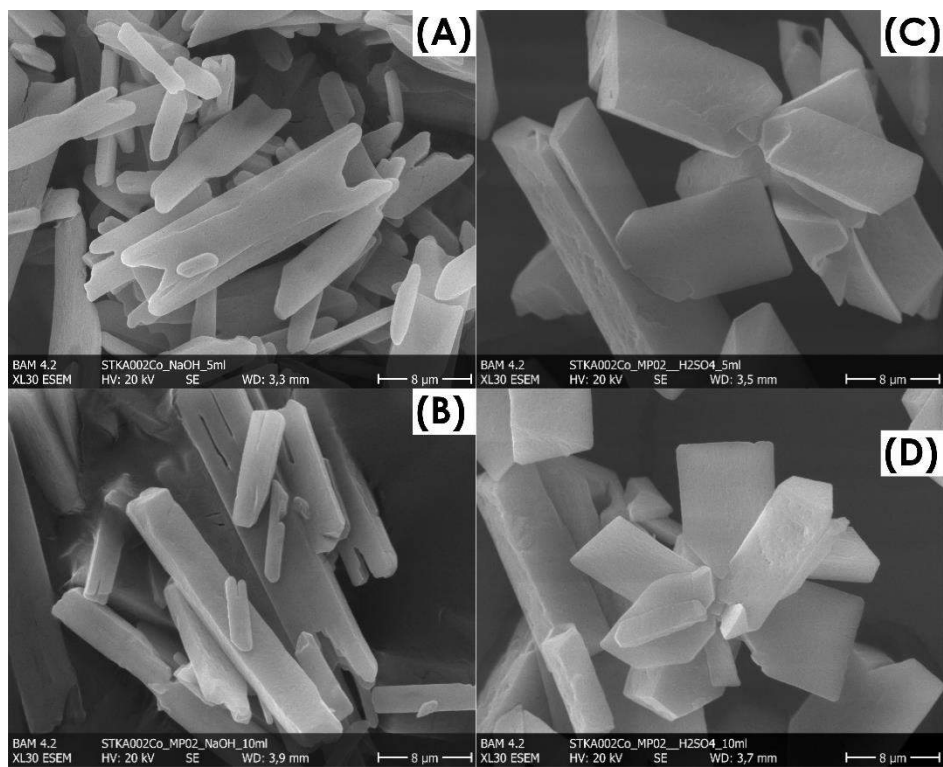


Figure S10: Co-struvite synthesized from 0.02 M Co and 0.1 M DAP leading to a M/P ratio of 0.2 at different initial pH with 5 ml and 10 ml 1 M NaOH_(aq) or 0.1M H₂SO_{4(aq)}; (A) 5 ml 1 M NaOH_(aq); (B) 10 ml 1 M NaOH_(aq); (C) 5 ml 1 M H₂SO_{4(aq)}; (D) 10 ml 1 M H₂SO_{4(aq)}.

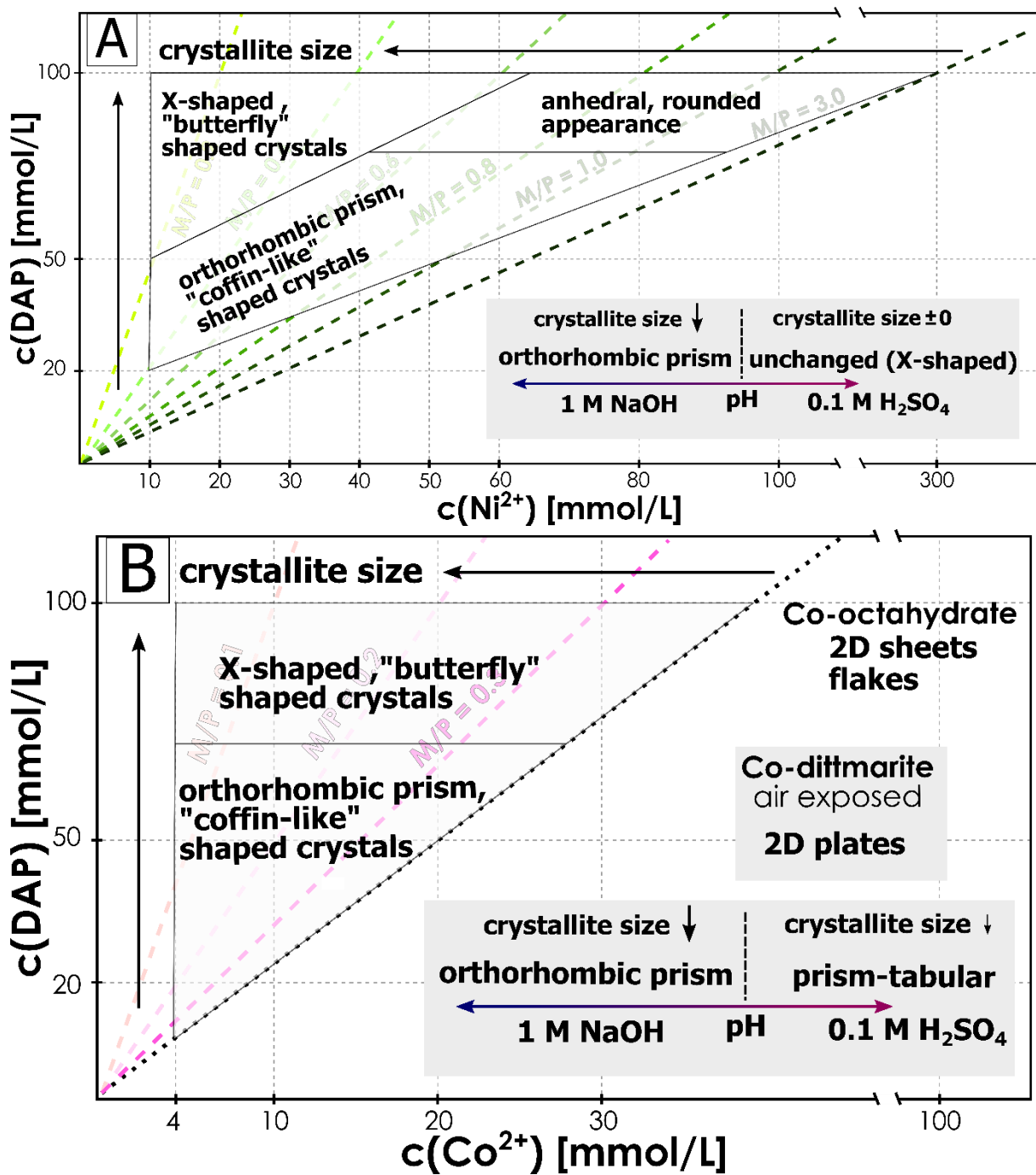


Figure S11: Crystallization trends in the $c(\text{M}^{2+})$ vs. $c(\text{DAP})$ plots with (A) green (for Ni) and (B) pink (for Co) dotted lines indicating the distinct M/P ratio of the sample. Crystal morphology fields are displayed in the triangles. The crystallite size increases with higher DAP and lower M^{2+} contents (see direction of the arrows); Adding $\text{NaOH}_{(\text{aq})}$ decreased the crystallite size and favored the formation of orthorhombic prisms. Co-octahydrate exhibits a 2D sheet or flake morphology. Co-dittmarite (formed due to air exposure) shows a 2D plate habit. In the Ni-system the crystallite size remained unchanged and while in the Co-system the crystals decreased slightly in size and habit to more tabular-shaped crystals.

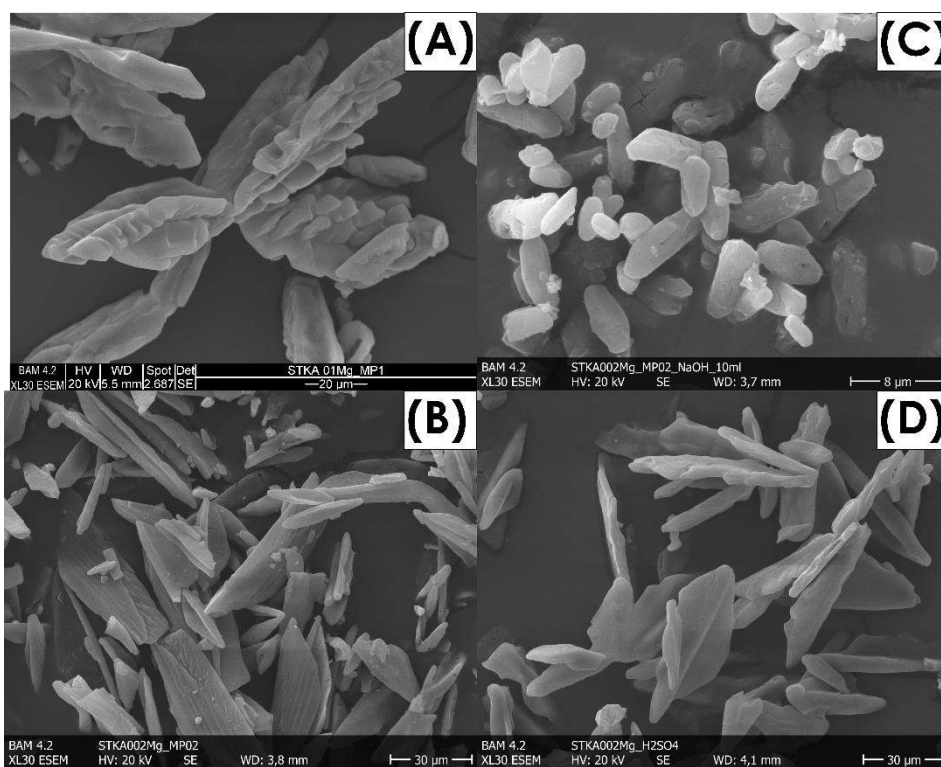


Figure S12: Mg-struvite crystals synthesized (A) at high 0.1 M Mg, 0.1 M DAP, M/P ratio = 1 and (B) low concentrations 0.02 M Mg, 0.1 M DAP, M/P ratio = 0.2 and pH adjusted low concentration samples with 10 ml of (C) sodium hydroxid NaOH_(aq) or (D) sulfuric acid H₂SO_{4(aq)}.

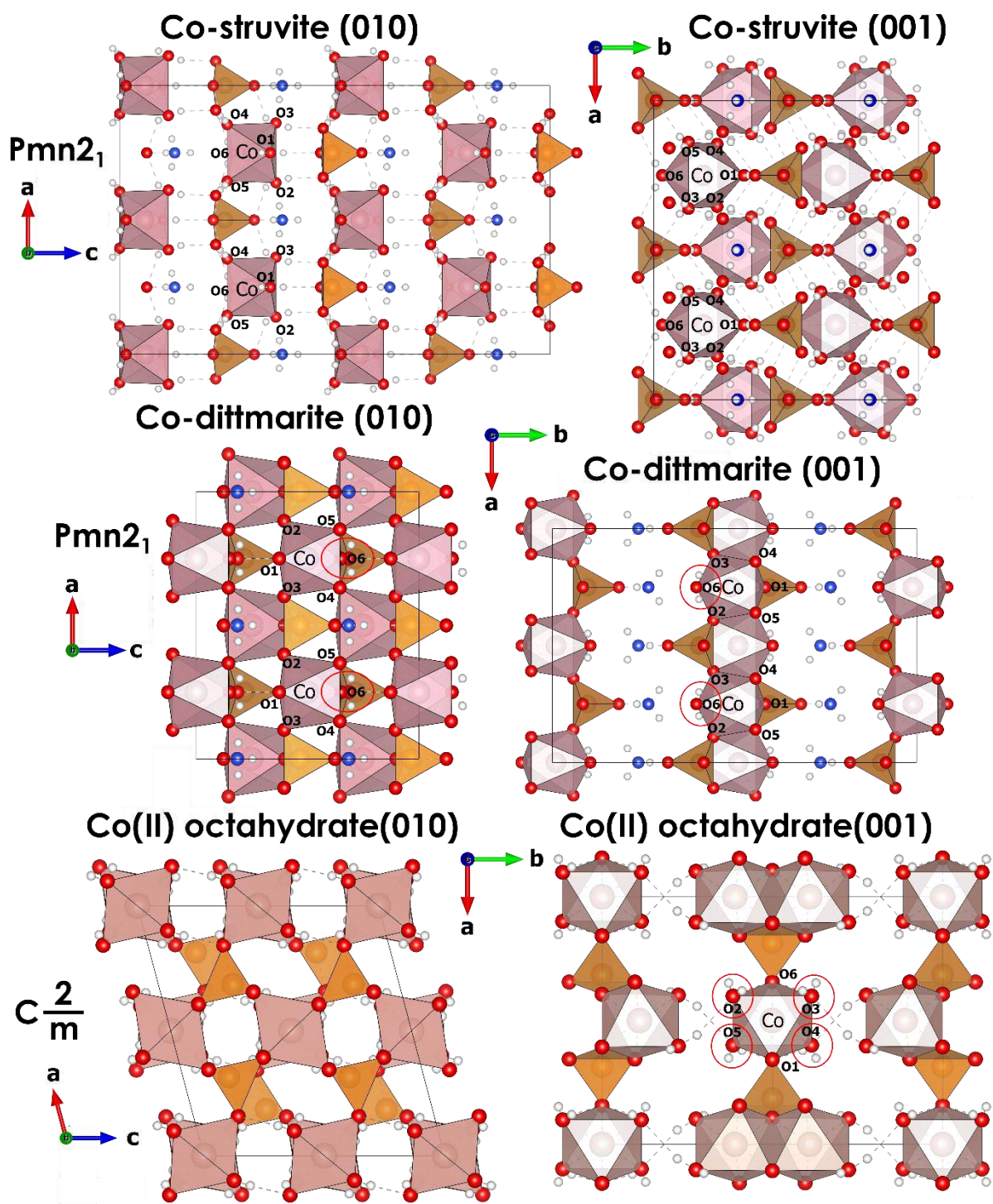


Figure S13: The (010) and (001) crystal planes of Co-struvite $NH_4CoPO_4 \cdot 6H_2O$, Co-dittmarite $NH_4CoPO_4 \cdot H_2O$ and Co(II)phosphate octahydrate $Co_3(PO_4)_2 \cdot 8H_2O$ crystal structure is displayed with the respective space group $Pmn2_1$ for Co-struvite and Co-dittmarite (orthorhombic) and space group $C2/m$ (monoclinic); Co: light pink, P: orange, O: red; N: blue and H: white; one or two exemplary CoO_6 octahedrons are marked by atom labels with all the coordinating oxygen numbered; the coordinating crystal water in Co-dittmarite and Co-octahydrate is marked with red ellipsoids; note that in the Co-dittmarite and Co-octahydrate structures, the CoO_6 is linked to the phosphate tetrahedrons, while in the Co-struvite structure the CoO_6 is isolated by six coordinating crystal water oxygens.

Supplementary Note

Cobalt is classified as a CRM according to the EU, because it is used in a number of technological applications, but it is only exploitable in few ore deposits in the world, mostly located in the Democratic Republic of the Congo. There, it is concentrated in minerals such as the cobaltite (CoAsS), erythrite ($\text{Co}_3(\text{AsO}_4)_2 \cdot 8\text{H}_2\text{O}$) or skutterudite (CoAs_3) in hydrothermal altered mantle rocks in association with mainly nickel. Although, it also plays an essential role in several enzymes and co-enzymes involved in the metabolism of animals and plants for example vitamin B12 (cobalamin), at above-trace concentrations cobalt is highly toxic.

Nickel is widely used in the industry and is also relatively common. It is mined in lateritic ultramafic rocks from ore minerals like pentlandite ($(\text{Ni,Fe})_8\text{S}_9$) or nickel ferrous limonite ($(\text{Ni,Fe})\text{O}(\text{OH})$). Unfortunately, in the environment nickel compounds cause numerous carcinogenic effects in human and plants and it is one of the most common allergens in the world. This is even though at trace concentrations it also plays an important biological role for plants and microbes as a part of enzymes such as urease^{11,12}. Hence although nickel is not a CRM, it should be recovered from wastewater.

In mining waters of the Eshidiya mine (Jordan) the PO_4^{3-} and NH_4^+ content ranges from 0.1 - 8.9 mg/l and 0.03 - 0.95 mg/l, respectively⁵. The related ground water in the same region showed concentrations values of PO_4^{3-} and NH_4^+ at 3.5-3.8 and 0.01-0.05 mg/l. Mine wastewaters from the Duluth Gabbro complex in Minnesota (USA) contain average values of 198 mg/l of Ni and 9.8 mg/l of Co⁴. In the Katanga province (DRC) in effluent surface mine waters of a Co-Cu ore deposit Co reached maximum concentrations of 3.16 mg/l¹. In Rio Piscianas (Italy) the highly contaminated groundwater from mining activities in the 1990s had concentrations of 1.5-2.9 mg/l for Co and 3.0-4.6 mg/l for Ni². Ground water samples from the Amik plain (Turkey) contain in average 13 mg/l NH_4^+ , 87 mg/l Phosphorus, 13 $\mu\text{g/l}$ Co and 50 $\mu\text{g/l}$ Ni³.

These numbers prove that transition metals as well as ammonia and phosphate are common contaminants in ground and wastewaters (see Table S7). As mining wastewaters contain high amounts of transition metals (mg/l) at low pH (~4-5) while agricultural waste- and ground waters demonstrate high concentrations of phosphate and ammonium at medium to high pH (7-9) a mixture of both wastewaters could lead to precipitation of M-struvite in significant amounts. By mixing different wastewaters together multiple environmental critical compounds could be extracted simultaneously. Further experiments to the up scalability and implementation as wastewater treatment method would quantitatively evaluate if the precipitation of M-struvite is applicable as wastewater treatment method or not.

References SI

1. Atibu, E. K.; Devarajan, N.; Thevenon, F.; Mwanamoki, P. M.; Tshibanda, J. B.; Mpiana, P. T.; Prabakar, K.; Mubedi, J. I.; Wildi, W.; Poté, J., Concentration of metals in surface water and sediment of Luilu and Musonoie Rivers, Kolwezi-Katanga, Democratic Republic of Congo. *Applied Geochemistry* **2013**, *39*, 26-32.
2. Concas, A.; Arda, C.; Cristini, A.; Zuddas, P.; Cao, G., Mobility of heavy metals from tailings to stream waters in a mining activity contaminated site. *Chemosphere* **2006**, *63*, (2), 244-53.
3. Agca, N.; Karanlik, S.; Odemis, B., Assessment of ammonium, nitrate, phosphate, and heavy metal pollution in groundwater from Amik Plain, southern Turkey. *Environ Monit Assess* **2014**, *186*, (9), 5921-34.
4. Hammack, R.; Edenborn, H., the removal of nickel from mine wastes using bacterial sulfate reduction. *Proceedings American Society of Mining and Reclamation* **1991**, 97-108.
5. Al-Hwaiti, M. S.; Brumsack, H. J.; Schnetger, B., Suitability assessment of phosphate mine waste water for agricultural irrigation: an example from Eshidiya Mines, South Jordan. *Environmental Earth Sciences* **2016**, *75*, (3).
6. Sracek, O.; Mihaljevič, M.; Kříbek, B.; Majer, V.; Veselovský, F., Geochemistry and mineralogy of Cu and Co in mine tailings at the Copperbelt, Zambia. *Journal of African Earth Sciences* **2010**, *57*, (1-2), 14-30.
7. Feng, C.; Zhang, S.; Wang, Y.; Wang, G.; Pan, X.; Zhong, Q.; Xu, X.; Luo, L.; Long, L.; Yao, P., Synchronous removal of ammonium and phosphate from swine wastewater by two agricultural waste based adsorbents: Performance and mechanisms. *Bioresour Technol* **2020**, *307*, 123231.
8. Leite, V.; Athayde Junior, G.; Sousa, J.; Lopes, W.; Henrique, I., Treatment of Domestic Wastewater in Shallow Waste Stabilization Ponds for Agricultural Irrigation Reuse. *Journal of Urban and Environmental Engineering* **2009**, *3*, (2), 58-62.
9. Percival, J.; Dumaresq, C.; Kwong, Y.; Hendry, K.; Michel, F., Arsenic in surface waters, Cobalt, Ontario. *Current Reserach 1996-C* **1996**, 137-146.
10. Stopic, S.; Pavlovic, J.; Friedrich, B., treatment of Highly Contaminated Waste Waters in a Continous Cascade Line Reactor. *World of metallurgy - ERZMETALL* **2007**, *60*, 255-262.
11. Carter, E. L.; Flugga, N.; Boer, J. L.; Mulrooney, S. B.; Hausinger, R. P., Interplay of metal ions and urease. *Metallomics* **2009**, *1*, (3), 207-21.
12. Mazzei, L.; Musiani, F.; Ciurli, S., The structure-based reaction mechanism of urease, a nickel dependent enzyme: tale of a long debate. *J Biol Inorg Chem* **2020**, *25*, (6), 829-845.